Functional divergence of Capicua isoforms explains differential tissue vulnerability in neurological disease

Hamin Lee[1,2,3], Esmeralda Villavicencio Gonzalez[1,2,3], Elias M. Rivera[2,3], Mark A. Durham[2,3,4,5], Ronald Richman[2,3], Elizabeth H.-Y. Chu[2,3], Kailey Xia[2,3], Hu Chen[3,6], Zhandong Liu[3,6], Surabi Veeraragavan[2,3], Binoy Shivanna[7], Huda Y. Zoghbi[1,2,3,4,6,7,8,9,10*]

[1]Program in Genetics and Genomics, Baylor College of Medicine, Houston, TX 77030, USA

[2]Department of Molecular and Human Genetics, Baylor College of Medicine, Houston, Texas 77030, USA.

[3]Jan and Dan Duncan Neurological Research Institute at Texas Children's Hospital, Houston, Texas 77030, USA

[4]Program in Developmental Biology, Baylor College of Medicine, Houston, TX 77030, USA

[5]Medical Scientist Training Program, Baylor College of Medicine, Houston, TX 77030, USA

[6]Department of Pediatrics, Baylor College of Medicine, Houston, Texas 77030, USA

[7]Department of Pediatrics, Texas Children's Hospital, Baylor College of Medicine, Houston, TX 77030, USA

[8]Department of Neuroscience, Baylor College of Medicine, Houston, TX 77030, USA

[9]Howard Hughes Medical Institute, Baylor College of Medicine, Houston, TX 77030, USA

[10]Lead contact

[*]Correspondence: hzoghbi@bcm.edu

ABSTRACT

Many neurological diseases impact specific brain regions despite widespread expression of the disease-related protein. Spinocerebellar ataxia type 1 (SCA1) primarily affects the cerebellum, though Ataxin-1 (ATXN1) is widely expressed. We previously showed that intensified interaction between mutant ATXN1 and Capicua (CIC) drives SCA1 pathogenesis in the cerebellum, whereas ATXN1 loss augments amyloid beta production in the hippocampus and cortex. CIC, however, forms a complex with ATXN1 and its paralog, Ataxin-1-like (ATXN1L)—yet knockout of either yields completely different phenotypes. To determine whether this could be due to CIC having two isoforms, we generated mice bearing either the long (CIC-L) or short (CIC-S) isoform. Loss of CIC-L led to cognitive deficits, whereas loss of CIC-S caused perinatal lethality, phenocopying, ATXN1 and ATXN1L knockout mice, respectively. Furthermore, CIC-L preferentially interacts with ATXN1, and CIC-S with ATXN1L. Our data underscore the importance of isoform–paralog interplay in studying regional vulnerability in neurodegenerative diseases.

INTRODUCTION

One of the puzzling features of many neurological diseases is that they seem to affect particular brain regions or cell types even though the disease-related protein is expressed widely throughout the brain and often in other tissues as well (Fu et al. 2018; Kampmann 2024). Typically, the disease ramifies outward from that locus of initial damage: Alzheimer's, for example, first targets the entorhinal cortex and hippocampus, whereas Parkinson's disease centers on the substantia nigra (Fu et al. 2018; Kampmann 2024). The same regional specificity is seen in Mendelian disorders as well, which allow us to more readily trace their developmental origins. For example, spinocerebellar ataxia type 1 (SCA1) is caused by expansion of a polyglutamine repeat tract in the gene *ATAXIN-1* (*ATXN1*) (Orr et al. 1993; Banfi et al. 1994). The ATXN1 protein is a transcriptional co-repressor that is expressed throughout the central nervous system (CNS) in both neurons and glia and is also expressed in organs such as the heart and liver (Servadio et al. 1995). In the CNS, it is most abundant in hippocampal pyramidal cells and cerebellar Purkinje cells, yet SCA1 pathology is largely restricted to the Purkinje cells and brainstem (Zoghbi and Orr 1995). Interestingly, a lack of ATXN1 does not cause ataxia but rather learning and memory deficits (Matilla et al. 1998; Crespo-Barreto et al. 2010; Asher et al. 2020): copy number variation of *ATXN1* is associated with Alzheimer's disease risk (Swaminathan et al. 2011; Swaminathan et al. 2012), and *Atxn1* knock-out in mice potentiates amyloid beta production (Suh et al. 2019). If, however, we delete *Atxn1* and its paralog, *Ataxin-1*-like (*Atxn1l*), the double mutant mice develop quite a different constellation of abnormalities that includes hydrocephalus, omphalocele, lung defects, and perinatal lethality (Lee et al. 2011). Loss of *Atxn1l* by itself causes the same phenotypes but with reduced penetrance (Lee et al. 2011).

It is reasonable to assume that this combination of regional specificity independent of expression level and the very different tissues affected by loss of ATXN1L indicates that ATXN1 and ATXN1L have

60 different native interactors. It was rather surprising, then, to find that they both form a complex with the
61 transcriptional repressor Capicua (CIC) (Lee et al. 2011; Lu et al. 2017), and both proteins are critical
62 for maintaining CIC stability (Lam et al. 2006; Lee et al. 2011; Lu et al. 2017; Wong et al. 2020).
63 ATXN1 and ATXN1L share a conserved CIC-binding domain (Mizutani et al. 2005; Lam et al. 2006;
64 Kim et al. 2013) and can substitute for each other in binding to CIC, exhibiting partial functional
65 redundancy (Bowman et al. 2007; Crespo-Barreto et al. 2010; Lee et al. 2011). CIC is also broadly
66 expressed (Lee et al. 2011; Kim et al. 2015; Lu et al. 2017) and interacts with ATXN1 throughout the
67 brain (Lu et al. 2017); the effect of the polyglutamine expansion in mutant ATXN1 is to intensify the
68 effect of this interaction, leading to hyper-repression of CIC targets (Fryer et al. 2011; Coffin et al.
69 2023). The formation of the mutant ATXN1–CIC complex is necessary for Purkinje cell pathology in
70 SCA1 (Rousseaux et al. 2018; Coffin et al. 2023). On the other hand, loss of ATXN1 reduces CIC levels,
71 leading to derepression of CIC targets *Etv4* and *Etv5* (Suh et al. 2019). These transcription factors have
72 binding sites upstream of *Bace1* and increase its expression, which in turn promotes amyloidogenic
73 processing of amyloid precursor protein (APP) and may be a risk factor for Alzheimer disease (Suh et al.
74 2019). Notably, this upregulation occurs only in the cortex and hippocampus, not in the cerebellum (Suh
75 et al. 2019).

76 CIC has broad developmental roles in both the peripheral tissues and the CNS. In mice, complete
77 loss of CIC causes perinatal lethality, with hydrocephalus, omphalocele and impaired lung development
78 (Lee et al. 2011; Simon-Carrasco et al. 2017)—reminiscent of *Atxn1l* knockout (KO) mice. In humans,
79 heterozygous loss-of-function variants cause CIC haploinsufficiency syndrome (CHS), a
80 neurodevelopmental disorder characterized by intellectual disability, autism spectrum disorder (ASD),
81 attention deficit hyperactivity disorder (ADHD), and seizures (Lu et al. 2017). Dual loss of both
82 ATXN1 and ATXN1L phenocopies the complete loss of CIC (Lee et al. 2011), and conditional KO in the

83 brain causing a CHS-like phenotype (Lu et al. 2017). How do these two paralogs, both acting through
84 CIC, produce such distinct loss-of-function outcomes?
85 We hypothesized that the answer might arise from the fact that CIC exists in two isoforms
86 generated by alternative promoter usage, namely, CIC-L (long) and CIC-S (short) (Lam et al. 2006).
87 Both isoforms share the HMG box and C1 DNA-binding domains as well as the ATXN1/ATXN1L-
88 binding domain (ATXN1/1L-BD) (Lam et al. 2006; Jimenez et al. 2012; Lee 2020). The functions of the
89 isoform-specific N-termini remain largely undefined, leaving open the possibility that the two isoforms
90 have distinct biological roles. To determine whether isoform-specific functions contribute to the regional
91 specificity of ATXN1 and ATXN1L gain- or loss-of-function phenotypes, we generated CIC isoform-
92 specific KO mice, characterized their phenotypes, and evaluated transcriptomic changes. We then
93 performed biochemical studies to assess the formation of different complexes. We found that,
94 surprisingly, subtle differences in the relative abundance of CIC isoforms and ATXN1 paralogs at the
95 protein level, together with the differential complexes they assemble, can dictate regional vulnerability.
96

97 **RESULTS**

98 **CIC isoforms and ATXN1/ATXN1L show different spatiotemporal expression patterns**

99 To investigate how the expression patterns of CIC isoforms relate to that of the CIC–ATXN1/1L
100 complex, we profiled protein levels of each CIC isoform together with ATXN1 and ATXN1L in the
101 cortex, cerebellum, and lung, of wild-type (WT) mice at four developmental stages: birth (P0), postnatal
102 day 6 (P6), postnatal day 21 (P21), and 12 weeks (**Fig. 1A, B**). These regions and developmental
103 timepoints were selected based on prior evidence of tissue-specific changes due to disruption of the
104 CIC–ATXN1/1L complex: in the forebrain, *Cic* knockout (KO) or *Atxn1/Atxn1l* double KO in mice
105 leads to selective reduction of cortical layers 2–4 beginning around postnatal day 5 (P5), with behavioral

106 abnormalities emerging by 3 months of age (Lu et al. 2017). In the lung, *Atxn1l* KO in mice disrupts the
107 transcriptional program of early alveolarization at P6 and results in reduced survival by P21 (Lee et al.
108 2011). The cerebellum, which is highly sensitive to ATXN1 gain-of-function toxicity, was included as a
109 comparator to these loss-of-function–vulnerable tissues (Rousseaux et al. 2018).

110 ATXN1L and both CIC isoforms showed a similar pattern of expression in the lungs, with the
111 highest levels at P6 and decreasing at later timepoints, whereas ATXN1 expression decreases over time
112 after P0 (**Fig. 1A, B**). Notably, ATXN1L levels are considerably higher in the lungs compared to the
113 cortex and cerebellum, with peak expression at P6. In the cortex, CIC-L and CIC-S expression patterns
114 diverged after P6, as reflected in a marked increase in the CIC-L/CIC-S ratio: CIC-L showed a slight
115 increase at P21 that was maintained at 12 weeks, while CIC-S markedly decreased between P6 and P21
116 and remained low at 12 weeks (**Fig. 1A-C**). In the cerebellum, all four proteins showed a pronounced
117 increase from P6 to P21, followed by a decrease in CIC-S and ATXN1L at 12 weeks. In 12-week-old
118 brains, we also looked at the hippocampus, striatum, and brainstem and found that both CIC isoforms
119 were most highly expressed in the cerebellum and least expressed in the brainstem (**Supplemental Fig.
120 S1**).

121 Thus, CIC, ATXN1, and ATXN1L show distinct tissue- and isoform-specific expression patterns
122 in mice from birth through young adulthood.

123

124 **CIC-S is critical for survival and for lung alveolarization**

125 To dissect the individual roles of each CIC isoform, we used CRISPR/Cas9 to generate *Cic-L*- and
126 *Cic-S*-specific KO mice by targeting the unique first coding exon of each isoform. For *Cic-S*-KO, we
127 targeted *Cic-S* exon 1 with a single guide RNA (sgRNA) and selected founder lines with deletions that
128 removed the in-frame downstream ATG (**Fig. 2A, Supplemental Fig. S2A**, **B**). For *Cic-L*-KO, we used

129 two sgRNAs to introduce a deletion within exon 2, resulting in a frameshift mutation and selective
130 disruption of the long isoform. We confirmed the deletions by Sanger sequencing (**Supplemental Fig.**
131 **S2C**) and used western blot to validate complete loss of either CIC-L or CIC-S in homozygous KO
132 animals (**Fig. 2B**). Interestingly, CIC-S protein levels are increased in *Cic-L*-KO, whereas loss of CIC-S
133 does not produce a comparable increase in CIC-L. CIC has been reported to bind regulatory regions of
134 its own locus (Weissmann et al. 2018), raising the possibility that there are isoform-specific differences
135 in transcriptional autoregulation of the CIC locus.

136 Since germline KO of *Cic* results in perinatal lethality (Lu et al. 2017; Simon-Carrasco et al.
137 2017), we sought to determine how loss of each isoform affects survival. We used chi-square analysis to
138 compare observed genotype frequencies to the expected Mendelian ratios of WT (25%), heterozygous
139 KO (50%), and KO (25%) at postnatal days 0, 6, and 21 (P0, P6, and P21; **Tables 1** and **2**). Both *Cic-S*
140 and *Cic-L*-KO animals exhibited the expected Mendelian ratios at P0, indicating no embryonic lethality.
141 At P6, neither group showed significant deviation from expected ratios, but by P21, approximately 70%
142 of *Cic-S*-KO had died (chi-square analysis, $p = 0.007$; **Table 1**) while *Cic-L*-KO animals maintained
143 normal survival (chi-square analysis, $p = 0.74$; **Table 2**).

144 We measured the weight and lifespan of surviving animals beyond P21. *Cic-S*-KO and *Cic-L*-KO
145 mice weighed less than WT throughout the 9-week period, although *Cis-S*-KO stopped gaining weight
146 around week 7 while *Cic-L*-KO mice continued to grow, reaching near WT weight by week 9 (**Fig. 3A**).
147 *Cic-S*-KO mice exhibited significant early lethality after 3 weeks, with 60% (15 of 25 animals) dying
148 before 20 weeks, whereas *Cic-L*-KO animals did not display reduced survival (**Fig. 3B**). Among the *Cic-*
149 *S*-KOs that died, 80% developed hydrocephalus accompanied by kyphosis, emaciation, and lethargy
150 prior to death. One animal experienced spontaneous and ultimately fatal home-cage seizures (**Fig. 3C**).
151 The remaining two animals that died without clear hydrocephalus or seizures showed further weight loss

152 beyond their already reduced baseline prior to death. Some *Cic-S*-KO mice survived up to 40 weeks
153 without any of these features, however, suggesting incomplete penetrance. Neither *Cic-L*-KO nor WT
154 animals developed any noticeable phenotype during this period.

155 These abnormalities of the *Cic-S*-KO mice are strongly reminiscent of those previously reported
156 in *Atxn1l*-KO mice (hydrocephalus with incomplete penetrance, lower body weight compared to WT
157 controls, and reduced survival by P21) (Lee et al. 2011). Because *Atxn1l*-KO mice also have impaired
158 alveolarization mediated by loss of CIC function that dysregulates extracellular matrix (ECM)
159 remodeling and alveolarization during late alveolarization stage (P17–P23), which was also present in
160 another line of mice bearing a *Cic* loss-of-function allele (Lee et al. 2011), we performed hematoxylin
161 and eosin (H&E) staining of lung tissue at P21 and quantified the mean linear intercepts (MLI). Despite
162 potential survivor bias in *Cic-S*-KO animals at this stage, the MLI values were significantly greater in
163 *Cic-S*-KO lungs than in WT littermates (*Cic-S*-KO, 29.73 ± 1.05 vs. WT littermate, 25.86 ± 0.71;
164 p=0.038, unpaired t-test; **Fig. 3D**) whereas MLI values of *Cic-L*-KO lungs were comparable to WT
165 littermate controls (*Cic-L*-KO, 27.21 ± 1.36 vs. WT littermate, 28.14 ± 1.17; p=0.658 , unpaired t-test;
166 **Fig. 3E**). Therefore, loss of CIC-S, but not CIC-L, impairs alveolarization, supporting functional overlap
167 between CIC-S and ATXN1L.
168

169 **CIC-L is crucial for neurobehavioral function**

170 Given the critical role of CIC in neurodevelopment (Lu et al. 2017; Ahmad et al. 2019; Hwang et
171 al. 2020), we performed a battery of behavioral assays in *Cic-S*-KO, *Cic-L*-KO, and WT littermates to
172 assess anxiety-like behavior, general locomotor activity, motor coordination, and social interaction—
173 phenotypes previously linked to CIC dysfunction in both people with CHS and in mouse models (Lu et
174 al. 2017; Tan and Zoghbi 2019). *Cic-L*-KO mice displayed reduced anxiety-like behavior in the elevated

175 plus maze assay, spending significantly more time in the open arms (**Fig. 4A**), and hyperactivity in the
176 open field test, with increased total distance traveled and higher speed compared to controls (**Fig. 4B**).
177 They had a shorter latency to fall from the rotarod (**Fig. 4C**) and took more time to descend in the pole
178 test (**Fig. S3A**). In the fear-conditioning assay, *Cic-L*-KO mice showed deficits in learning and memory,
179 freezing less in both contextual (**Fig. 4D**) and cued fear tests (**Fig. 4E**). In the three-chamber assay, both
180 KO lines preferred to interact with the conspecific than the object (**Fig. S3B**).

181 *Cic-S*-KO mice exhibited minimal behavioral abnormalities (**Fig. 4A-C**). The only significant
182 phenotype that *Cic-S*-KO mice displayed was increased freezing in the contextual test (**Fig. 4D**) and pre-
183 tone in the cued test (**Fig. 4E**), which do not signify any learning or memory deficit. These data suggest
184 that, for the animals that survive because of decreased penetrance, CIC-S is not critical for most
185 neurobehavioral functions, with only mild effects on baseline freezing behavior.

186 *Cic-L*-KO mice phenocopied *Atxn1*-KO mice, which show learning deficits (Matilla et al. 1998;
187 Crespo-Barreto et al. 2010; Asher et al. 2020). Collectively, the survival and neurobehavioral data point
188 to a functional and spatio-temporal convergence between CIC-L and ATXN1 on the one hand, and CIC-
189 S and ATXN1L on the other.

190

191 **Region-specific transcriptomic overlap between CIC isoform and ATXN1 paralog KOs**

192 To determine whether phenotypic similarities between these two pairs of mouse lines reflect
193 shared transcriptional changes, we performed bulk RNA sequencing (RNA-seq) on tissues linked to the
194 phenotype of each CIC isoform loss (P6 lung and 12-week cortex) and compared the differentially
195 expressed genes (DEGs) previously identified in *Atxn1*-KO and *Atxn1l*-KO mice. We used the
196 cerebellum as an internal control, since it does not contribute to the CHS phenotype despite its great
197 sensitivity to polyglutamine-expanded ATXN1 (Rousseaux et al. 2018)

198 In the P6 lung, *Cic-S*-KO samples exhibited a greater number and magnitude of DEGs (*p*-adjusted
199 < 0.05 and |log2 fold change (Log2FC)| > 0.25) than *Cic-L*-KO, with enrichment of upregulated genes
200 consistent with CIC's role as a transcriptional repressor (**Supplemental Fig. S4A**, **B**). These differences
201 aligned with more pronounced survival and developmental phenotypes in *Cic-S*-KO animals (**Table 1**,
202 **Fig. 3**). Gene set enrichment analysis (GSEA) (Subramanian et al. 2005) revealed distinct GO term
203 enriched for each isoform KO, with *Cic-S*-KO enriched for immune-related terms (**Supplemental Fig.**
204 **S4C**) and *Cic-L*-KO for chromosome segregation-related terms (**Supplemental Fig. S4D**).
205 Consistent with the phenotypic similarities, the *Cic-S*-KO DEGs showed stronger overlap with the
206 *Atxn1l*-KO DEGs (Lee et al. 2011) (Fisher's exact test, OR = 19.85, $p = 6.32 \times 10^{-132}$; **Supplemental**
207 **Fig. S5A**) than *Cic-L*-KO (OR = 3.58, $p = 1.7 \times 10^{-12}$; **Supplemental Fig. S5B**), with most shared genes
208 showing concordant expression changes. Interestingly, although *Atxn1*-KO lungs had only 34 DEGs, just
209 over a third overlapped with the *Cic-S*-KO DEGs (OR = 4.74, $p = 5.83 \times 10^{-5}$; **Supplemental Fig. S5C**)
210 or the *Cic-L*-KO DEGs (Fisher's exact test, OR = 9.86, $p = 8.54 \times 10^{-8}$; **Supplemental Fig. S5D**). Given
211 the role of the *Etv–Mmp* axis in *Atxn1l*-KO alveolarization defects (Lee et al. 2011) and the fact that
212 *Etv1/4/5* are direct CIC targets (Dissanayake et al. 2011; Lee et al. 2011; Weissmann et al. 2018; Coffin
213 et al. 2023), we examined their expression specifically. *Etv4, Mmp8, Mmp9,* and *Mmp12* were strongly
214 upregulated in *Cic-S*-KO lungs, while *Etv4, Mmp12* and *Mmp13* showed mild upregulation in *Cic-L*-KO
215 (**Supplemental Fig. S5E**). GSEA revealed enrichment of extracellular matrix (ECM) assembly-related
216 pathways in *Cic-S*-KO, whereas *Cic-L*-KO showed weak or non-significant enrichment (**Supplemental**
217 **Fig. S5F**). These results suggest that CIC-S and ATXN1L regulate similar genes in the lung during lung
218 development.
219 In the 12-week-old cortex, there were more DEGs in the *Cic-L*-KO with larger fold-changes than
220 in *Cic-S*-KO (**Supplemental Fig. S6A, B**). Whereas *Cic-S*-KO top GSEA terms were mostly related to

221 glia or to bioenergetics (**Supplemental Fig. S6C, D**), *Cic-L*-KO terms involved synapse and
222 neurotransmission-related functions (**Supplemental Fig. S6E, F**). Comparison with *Atxn1*-KO cortex
223 DEGs (*unpublished data*) revealed greater overlap and stronger enrichment with *Cic-L*-KO than *Cic-S*-
224 KO, with more genes changing in the same direction (**Supplemental Fig. S7A, B, Supplemental Table**
225 **S1, 2**). Enrichment analysis of these concordant DEGs showed that only *Cic-L*-KO shared synapse- and
226 memory-related GO terms with *Atxn1*-KO (**Supplemental Fig. S7C, D**). Consistent with previous
227 findings that the *Etv4/Etv5–Bace1* axis is upregulated in *Atxn1*-KO cortex (Suh et al. 2019), we
228 observed similar upregulation of this axis in *Cic-L*-KO cortex (**Supplemental Fig. S7E**). These findings
229 support the idea that CIC-L and ATXN1 regulate similar gene networks that underlie learning and
230 memory.

231 In the cerebellum, a region generally more resistant to the loss of the CIC–ATXN1/1L complex
232 but clearly vulnerable to the gain of CIC-ATXN1 function (Rousseaux et al. 2018; Coffin et al. 2023),
233 we observed fewer DEGs in *Cic-L*-KO compared to the cortex, but more DEGs in *Cic-S*-KO relative to
234 its cortical counterpart (**Supplemental Fig. S8A, B, Supplemental Table S3, 4**), potentially reflecting
235 higher CIC-S expression in this region at 12 weeks (**Supplemental Fig. S1**). The two KOs also showed
236 distinct GO term enrichments (**Supplemental Fig. S8C–F**), and DEG overlap with *Atxn1*-KO was
237 stronger for *Cic-S*-KO (Fisher's exact test, OR = 2.41, $p = 1.69 \times 10^{-17}$; **Supplemental Fig. S9A**) than
238 for *Cic-L*-KO (Fisher's exact test, OR = 1.61, $p = 2.85 \times 10^{-8}$; **Supplemental Fig. S9B**). *Etv4*, which
239 was strongly upregulated in the cortex of *Cic-L*-KO, showed less upregulation in the cerebellum,
240 whereas *Etv5* and *Bace1* remained unchanged (**Supplemental Fig. S9C**).

241 CIC-L and CIC-S, therefore, largely regulate different biological processes. Their respective
242 transcriptional convergences with ATXN1/1L are both region- and timepoint-dependent.
243

244 **CIC-S preferentially associates with ATXN1L, and CIC-L associates with ATXN1, in a region-**
245 **specific manner**

246 Given the region-specific transcriptomic overlap—between the cortex in *Cic-L*–KO and *Atxn1*–
247 KO mice, and the cerebellum in *Cic-S*–KO and *Atxn1*–KO mice—we sought to determine whether CIC
248 isoform–paralog pairs form distinct complexes across brain regions. We performed size exclusion
249 chromatography (SEC) on protein extracts from cortical and cerebellar tissue harvested from 2–3-
250 month-old *Cic-S*-KO and *Cic-L*-KO mice to examine the elution profiles of CIC, ATXN1, and ATXN1L.

251 In the WT cortex both ATXN1 and ATXN1L co-eluted with CIC in a high molecular weight
252 complex (~1.7 MDa, fraction 12), as well as in distinct smaller complexes (ATXN1 peaking at fraction
253 15, ~300 kDa; ATXN1L at fractions 16–17, ~170–88 kDa; **Fig. 5A, B**), consistent with prior reports (Lu
254 et al. 2017). In contrast, both *Cic-S*-KO and *Cic-L*-KO cortices showed less ATXN1 and ATXN1L in the
255 high molecular weight fractions and a concomitant increase in smaller fractions, suggesting that CIC is
256 essential for maintaining their incorporation into the larger complex (**Fig. 5A, B**). Interestingly, in *Cic-L*-
257 KO cortex, ATXN1 showed a stronger shift from the large to small complex (large-to-small complex
258 ratio: 0.41± 0.05, vs. WT 1.00± 0.08; $p = 0.003$, one-way ANOVA) than in *Cic-S*-KO (0.67± 0.08; p
259 $=0.039$) (**Fig. 5C**, left), indicating preferential association of ATXN1 with CIC-L. In contrast, in *Cic-S*-
260 KO cortex ATXN1L shifted markedly to smaller fractions (0.11± 0.03, vs. WT 1.00± 0.03; $p = 0.0001$)
261 and was nearly absent from the large complex. This shift was less pronounced in *Cic-L*-KO (0.51± 0.13;
262 $p = 0.006$; **Fig. 5C**, right), suggesting a stronger association of ATXN1L with CIC-S. This redistribution
263 does not appear to be driven by changes in total protein levels: ATXN1 is lower in *Cic-S*-KO compared
264 to WT, yet the reduction in the large complex is greater in *Cic-L*-KO. ATXN1L levels are not
265 significantly different in either isoform knockout compared to WT (**Supplemental Fig. S10A**). These
266 findings confirm isoform-specific associations within the CIC–ATXN1/ATXN1L complex in the cortex.

267 In the *Cic-S*-KO cerebellum, ATXN1L shifted markedly toward smaller fractions (0.07± 0.03, vs.
268 WT 1.00± 0.08; $p = 0.0002$). The shift was more modest in *Cic-L*-KO (0.63± 0.13; $p = 0.042$; **Fig. 5D–**
269 **F**), consistent with its preferential association with CIC-S observed in the cortex. In contrast to the
270 cortex, ATXN1 also shifted in *Cic-S*-KO cerebellum (0.42± 0.06, vs. WT 1.00± 0.17; $p = 0.015$), while
271 its distribution remained largely unchanged in *Cic-L*-KO (0.90± 0.11; $p = 0.82$; **Fig. 5D-F**). As in the
272 cortex, changes observed in the cerebellum do not appear to be driven by ATXN1 or ATXN1L levels, as
273 their expression is not significantly altered in either isoform knockout compared to WT **(Supplemental**
274 **Fig. S10B)**.
275 The cerebellum has the highest level of CIC-S among all brain regions, as well as the highest total
276 CIC expression (**Supplemental Fig. S1A–D**). ATXN1 is expressed at lower levels, however, resulting in
277 the highest CIC-to-ATXN1 ratio in the cerebellum (**Supplemental Fig. S1E**), which may lead to a
278 greater proportion of ATXN1 bound to CIC. Supporting this hypothesis, comparison of WT cerebellar
279 and cortical SEC patterns (**Supplemental Fig. S11**) revealed a striking difference: the cerebellum
280 exhibits a higher proportion of ATXN1 in the large complex and lower levels in the small complex
281 (**Supplemental Fig. S11C**), a pattern not observed for ATXN1L (**Supplemental Fig. S11D**). The
282 relatively high CIC-S levels may explain why CIC-S is especially important for ATXN1 large complex
283 formation in the cerebellum. Moreover, the combination of a high CIC/ATXN1 ratio likely predisposes
284 the cerebellum to gain-of-function effects of the complex. It is worth noting that cerebellar single-
285 nucleus RNAseq (Kozareva et al. 2021) show that both *Cic* and *Atxn1* are highly expressed in Purkinje
286 cells, which are most vulnerable to SCA1 (**Supplemental Fig. S12**).
287 Overall, these results indicate that CIC isoforms and ATXN1 paralogs favor particular interactions
288 depending on the context. While the CIC-S–ATXN1L interaction appears strong and consistent across
289 regions, ATXN1 associates with different CIC isoforms in different tissues.

290

291 **The unique N-terminal of each CIC isoform mediates the ATXN1 paralog-specific interaction**

292 To understand the mechanism of isoform-specific complex formation of CIC with either ATXN1
293 or ATXN1L, we first examined the interaction of CIC-L and CIC-S with ATXN1 and ATXN1L by
294 performing coimmunoprecipitation (co-IP) assays in WT cortical lysates. Despite comparable expression
295 levels of CIC isoforms in the cortex, ATXN1 immunoprecipitation showed strong enrichment of CIC-L
296 relative to CIC-S (**Fig. 6A**). Conversely, ATXN1L immunoprecipitation demonstrated an even more
297 pronounced enrichment of CIC-S over CIC-L (**Fig. 6B**), which may explain the more prominent
298 ATXN1L shift observed in SEC (**Fig. 5A-C**). These results support the hypothesis that ATXN1
299 preferentially interacts with CIC-L, whereas ATXN1L favors CIC-S.

300 Since CIC-S and CIC-L share a canonical ATXN1/ATXN1L binding domain (ATXN1/1L-BD)
301 that can bind both ATXN1 and ATXN1L, we hypothesized that there should be isoform-specific binding
302 sites outside the ATXN1/1L-BD that mediate preferential interaction between CIC-S and ATXN1L, and
303 CIC-L and ATXN1. To test this possibility, we performed the analysis using human CIC, ATXN1, and
304 ATXN1L sequences. The W37A mutation in CIC-S has been previously shown to disrupt binding with
305 the AXH domain of ATXN1(Kim et al. 2013). Using the corresponding mutation in CIC-L (W946A), we
306 found that CIC-S W37A lost interaction with ATXN1 but CIC-L W946A retained ATXN1 binding (**Fig.
307 6C**). This suggests that CIC-L contains an additional ATXN1-binding region. We saw the opposite with
308 ATXN1L, despite CIC-S containing only 22 isoform-specific amino acids at its N-terminus: ATXN1L
309 still bound CIC-S W37A but failed to interact with CIC-L W946A (**Fig. 6D**). These data indicate that
310 distinct, noncanonical regions in each isoform mediate selective interactions with ATXN1 and ATXN1L.

311 To test whether the N-terminal region of CIC-L can mediate the selective interaction with
312 ATXN1, we expressed this region alone and performed co-IP. The CIC-L N-terminus, which spans 931

313 amino acids and does not contain the ATXN1/1L-BD, interacted with ATXN1 but not with ATXN1L
314 (**Fig. 6E, F**). Thus, the N-terminal region of CIC-L is sufficient to mediate interaction with ATXN1, but
315 not ATXN1L, and may thereby contribute to isoform-paralog specificity.
316 Together, these findings reveal a previously unrecognized mechanism by which CIC isoforms
317 interact with different ATXN1 paralogs through isoform-specific domains, establishing a novel
318 molecular basis for paralog-specific complex formation.
319

320 **CIC-L expression is more dependent on ATXN1 than CIC-S**

321 Given the preferential interaction between ATXN1 and CIC-L, and the known role of ATXN1 in
322 maintaining CIC protein stability (Lam et al. 2006), we hypothesized that CIC-L would be more
323 dependent on ATXN1. To test this, we measured CIC-L and CIC-S protein levels in WT and *Atxn1*-KO
324 mice across brain regions sensitive to ATXN1 loss (cortex, hippocampus) or gain (cerebellum,
325 brainstem). CIC-L levels were significantly lower in all four regions in *Atxn1*-KO mice, but CIC-S
326 levels were more modestly reduced, and only in the cerebellum (**Supplemental Fig. S13A-D**). The
327 cerebellar reduction in CIC-S was consistent with our SEC analysis showing a shift of CIC-S in ATXN1-
328 containing fractions (**Fig. 5D-F**). IP of ATXN1 confirmed a preferential association with CIC-L in all
329 brain regions examined (**Supplemental Fig. S13E**). These findings indicate that the cortical and
330 hippocampal abnormalities in *Atxn1*-KO mice may result primarily from the loss of CIC-L function.
331

332 **DISCUSSION**

333 The present study uncovers functionally distinct roles for the two CIC isoforms, CIC-L and CIC-
334 S. The overlap of transcriptomic changes in *Cic-S*-KO and *Atxn1l*-KO mice explains why these two lines
335 show the same early lethality, hydrocephalus, and lung alveolarization defects, while *Cic-L*-KO and

336 *Atxn1*-KO mice share learning and memory deficits. These phenotypic parallels reveal an unexpected
337 degree of specificity in CIC–ATXN1 complex formation, given that both isoforms share the canonical
338 ATXN1/ATXN1L binding domain (ATXN1/1L-BD); the specificity is attributable to the unique N-
339 terminal domains of each isoform that favor binding between CIC-S and ATXN1L, and between CIC-L
340 and ATXN1. The sharp distinctions between the two sets of phenotypes provide compelling *in vivo*
341 support of the idea that different isoforms greatly expand protein interaction capacities and may indeed
342 serve as "functional alloforms" (Yang et al. 2016).

343 Prior studies in *Drosophila* have shown that CIC isoforms play distinct roles during
344 development: Cic-S is critical for early embryogenesis through its interaction with Groucho (Fores et al.
345 2015), while Cic-L is essential for oogenesis (Rodriguez-Munoz et al. 2022). These findings support the
346 idea that the divergent N-terminal regions of CIC isoforms confer isoform- and context-specific
347 functions. However, *Drosophila* Cic-S has evolved on its own (Fores et al. 2015), with the species
348 possessing only Atx-1 (containing the AXH domain) and lacking the paralog pairs found in mammals.
349 Furthermore, there is no evidence for an endogenous functional complex between *Drosophila* Cic and
350 Atx-1. By using a mammalian system in which both CIC isoforms and ATXN1 paralogs are highly
351 conserved, we identified a previously unrecognized layer of regulation: isoform–paralog–specific
352 interactions.

353 These isoform-specific roles are not only of evolutionary interest but also carry direct clinical
354 relevance. Recently, a CIC-L–specific mutation was reported in a patient with CHS (Sharma et al.
355 2022), which is consistent with our finding that CIC-L is critical for neurological function. There may be
356 additional patients with CIC-L variants who remain unrecognized. Furthermore, given the role of CIC-L
357 in learning and memory and its regulation of the *Etv4/5–Bace1* axis, CIC-L variants could, like *ATXN1*
358 (Bertram et al. 2008; Bettens et al. 2010; Swaminathan et al. 2011; Swaminathan et al. 2012; Suh et al.

359 2019). contribute to susceptibility to Alzheimer's disease. More broadly, the expression of different
360 isoforms can be dysregulated in disease, but gene-level expression measures commonly used in biology
361 average the translational potential of each isoform and therefore may not accurately reflect protein
362 concentration. It has also been proposed that isoform-specific therapeutics would improve efficacy and
363 reduce adverse effects (Kjer-Hansen et al. 2024).

364 Our findings help resolve two longstanding questions: (1) What underlies the regional
365 vulnerability to loss or gain of the CIC–ATXN1 complex despite its broad expression? (2) How does the
366 loss of ATXN1 versus ATXN1L lead to distinct phenotypes, despite both acting through CIC? We
367 propose that the combination of isoform–paralog–specific interactions and regional expression patterns
368 determines the differential sensitivity to complex disruption. Consistent with this model, the similarity in
369 learning and memory deficits, along with upregulation of the *Etv4/5–Bace1* axis, in both *Atxn1*-KO and
370 *Cic-L*-KO mice suggests that these phenotypes arise from preferential CIC-L–ATXN1 complex
371 formation in the cortex and possibly the hippocampus.

372 Although we did not assess isoform-specific contributions to the cerebellar and brainstem
373 pathology seen in SCA1, the current study does shed light on this question. We find that total CIC levels
374 and CIC/ATXN1 ratios are highest in the cerebellum, with a greater proportion of ATXN1 being
375 incorporated into the large complex. Our prior work in SCA1 mice demonstrated that ~50% reduction of
376 total CIC (affecting both isoforms) (Fryer et al. 2011) or a polyQ-ATXN1 mutation that would abolish
377 binding to both isoforms fully rescues the Purkinje cell phenotype (Rousseaux et al. 2018; Coffin et al.
378 2023). These findings indicate that total CIC levels bound to ATXN1, rather than isoform identity, are
379 critical for Purkinje cell degeneration. By contrast, CIC expression is lowest in the brainstem, which
380 may be why loss of the ATXN1-CIC interaction does not fully rescue brainstem SCA1 phenotypes
381 (Fryer et al. 2011; Coffin et al. 2023) and why CIC motifs are less enriched in the brainstem's disease-

382 associated gene network (Friedrich et al. 2018). In SCA1, the brainstem's ATXN1 protein complex
383 composition is distinct from that in the cerebellum (Jafar-Nejad et al. 2011), indicating that brainstem
384 pathology arises through different mechanisms.

385 Our findings also allow us to draw some inferences that can be tested in the future. First, ATXN1
386 loss does not fully recapitulate CIC-L deficiency: transcriptomic comparisons reveal only partial overlap
387 between *Atxn1*-KO and *Cic-L*-KO datasets, indicating that ATXN1 and CIC-L have functions outside of
388 their shared complex. Indeed, ATXN1 has interactors beyond CIC (Chen et al. 2003; Tsuda et al. 2005;
389 Serra et al. 2006; Lim et al. 2008; Coffin et al. 2023), and such partners may act in compensatory
390 transcriptional or chromatin regulatory pathways, buffering CIC-dependent gene expression programs.

391 What are the ATXN1/ATXN1L-independent mechanisms that distinguish CIC-L from CIC-S? If
392 isoform differences were driven solely by interactions with ATXN1 and ATXN1L, *Cic-L*-KO and *Cic-S*-
393 KO transcriptomes would be expected to fully overlap, differing only in the magnitude of differential
394 expression. Instead, the partial overlap of DEGs may reflect isoform-specific interactors that influence
395 target gene selection. Alternatively, the isoforms may differ in cell type expression, affecting distinct
396 cellular populations. Divergent GO term enrichments support this notion. Profiling isoform-specific
397 expression across cell types and applying single-cell transcriptomics to each isoform KO will be critical
398 to dissect these contributions.

399 Finally, our findings highlight a broader principle that paralogous proteins and their isoform-
400 specific partners can form distinct regulatory complexes with completely different biological functions.
401 The CIC–ATXN1/1L complex may serve as a paradigm for understanding how paralog-isoform specific
402 interactions shape regional vulnerability and disease susceptibility in other diseases such as those
403 involving amyloid precursor protein (Kang et al. 1987; Kitaguchi et al. 1988; Ponte et al. 1988; Tanzi et
404 al. 1988; Wasco et al. 1992; Sprecher et al. 1993; Wasco et al. 1993), tau (Wang and Mandelkow 2016;

405 Chung et al. 2021), or α-synuclein (Rhinn et al. 2012), all of which exist within paralog families and

406 have multiple isoforms.

407

408 **MATERIALS AND METHODS**

409 **Mouse husbandry**

410 All mice were backcrossed to C57BL/6J background. All mice were housed and maintained in the
411 animal facilities at Baylor College of Medicine (BCM) on a 12-hour light-dark cycle. BCM Institutional
412 Animal Care & Use Committee (IACUC) approved all animal care and experimental procedures.

413

414 **HEK293T cell line**

415 Human embryonic kidney cell T (HEK293T) (ATCC, CRL-3216) were cultured in Dulbecco's modified
416 Eagle's medium (DMEM, Corning, MT10013CV) supplemented with 10% fetal bovine serum (Gibco
417 A4736201) and 1X antibiotic-antimycotic (Gibco, 15240096). Cell cultures were maintained at 37 °C in
418 a humidified 5% CO_2 incubator.

419

420 **Generation of *Cic-L*-KO and *Cic-S*-KO mice**

421 *Cic-L*-KO and *Cic-S*-KO alleles were generated using CRISPR/Cas9 genome editing. For *Cic-L*-KO,
422 two crRNAs targeting exon 2 of *Cic-L*, the first coding exon unique to the CIC-L isoform, were
423 designed (5′-CGCACCTGGCGCACGACTGC-3′ and 5′-TCCAGCCGCACCGACTGCTG-3′; IDT) to
424 generate a large deletion. For Cic-S-KO, a single crRNA targeting exon 1 of Cic-S was designed (5′-
425 ACGCGGGTATCAGGGGCCTG-3′; IDT).

426 crRNA, tracrRNA, and Cas9 protein were prepared as described previously (Coffin et al. 2023) with
427 modifications to total reaction volume, concentration and delivery method. Final concentrations were
428 6.6 μM crRNA, 6.6 μM tracrRNA, and 6 μM Cas9 in $T_{10}E_{0.1}$ buffer. For *Cic-L*-KO, each crRNA was

429 diluted to 3.3 μM. The mixture was electroporated into zygotes by the Genetically Engineered Rodent
430 Model (GERM) Core at Baylor College of Medicine (BCM).

431 Founders were screened by PCR using primers flanking the expected deletion sites (*Cic-L*-KO: 5′-
432 TCCTCCTCTACTGACACGGC-3′, 5′-TAGGACAAGCAGCTCATCACC-3′; *Cic-S*-KO: 5′-
433 GGCCAAGGAGCGGGTTAC-3′, 5′-TCCTAGTGCAGTACCGTCCA-3′). PCR products were TOPO
434 cloned (Invitrogen) and analyzed by Sanger sequencing for frameshift deletions. *Cic-S*-KO founders
435 were selected for deletions eliminating the downstream ATG in exon 1. Founder lines were backcrossed
436 to C57BL/6J WT mice (Jackson Laboratory), and germline transmission was confirmed by sequencing
437 of F1 progeny.

438 Immunoblotting was performed on homozygous KO animals to confirm the loss of the corresponding
439 CIC isoform. One independent founder line was established for each isoform KO and maintained by
440 successive backcrossing (>5 generations) to C57BL/6J prior to experimental use.

441

442 **Genotyping of *Cic-L*-KO and *Cic-S*-KO mice**

443 Genotyping was performed by PCR using allele-specific primers. For *Cic-L*, WT and KO alleles were
444 distinguished using two primer sets: *Cic-L*-WT (5′-ACTGGAGAAGGGAGCTGCAC-3′ and 5′-
445 CTGTCCCTCGAAGTCTCATCG-3′) and *Cic-L*-KO (5′-TCCTCCTCTACTGACACGGC-3′ and 5′-
446 TAGGACAAGCAGCTCATCACC-3′). For *Cic-S*, a single primer pair (5′-
447 GGCCAAGGAGCGGGTTAC-3′ and 5′-TCCTAGTGCAGTACCGTCCA-3′) was used, and WT versus
448 KO alleles were distinguished based on product size.

449

450 **Lung Histopathology**

451 The lungs were harvested for morphometry studies on postnatal day (P) 21, as described before
452 (Shrestha et al. 2019). Both lungs of the experimental mouse (n=3-5/group) were inflated at 25 cm
453 pressure for at least 10 minutes via tracheal cannulation with 4% paraformaldehyde. The inflated lungs
454 were then fixed overnight with 4% paraformaldehyde at room temperature with gentle agitation. The
455 fixed lungs were stored in 70% ethanol in a refrigerator until further processing for lung histopathology.
456 The lungs were then paraffin-embedded, sliced into 5 µm thin sections, and stained with H&E. We
457 examined at least five random non-overlapping fields of 10X H&E stained images from both lungs of
458 each animal to quantify alveolarization by mean linear intercepts (MLIs). To calculate the MLI, grids of
459 horizontal and vertical lines were placed on the H&E stained lung images, and the number of times the
460 lines intersected with the lung tissue was counted. The MLI was determined by dividing the total length
461 of the grid lines by the number of intersects.

462

463 **Behavioral Assays**

464 All behavioral analyses were conducted during the light phase of a 12-hour light-dark cycle by an
465 experimenter blinded to mouse genotype. Mice had *ad libitum* access to food and water except during
466 testing. Age-matched mice were used in all experiments, and wild-type (WT) littermates from both C*ic-*
467 *S*-KO and *Cic-L*-KO breeding were pooled as controls. Mice were habituated in the test room for at least
468 30 min prior to each assay. Tests were performed under room lighting of 150 lux with background white
469 noise at 60 dB.

470 **Elevated plus maze**: Mice (8-10 weeks of age) were placed in the center of an elevated plus maze
471 consisting of two open arms (25 × 8 cm, with 0.5 cm raised edges) and two closed arms (25 × 8 cm,

472 enclosed by 15 cm high walls), elevated 50 cm above the floor. Behavior was recorded for 10 min using
473 a camera and ANY-maze video tracking system (Stoelting, Wood Dale, IL, USA). Measures included
474 time spent, distance travelled and number of entries in open and closed arms.

475 **Open field assay**: Mice (9-11 weeks of age) were placed in the center of a 40 × 40 × 30 cm chamber
476 equipped with photobeams (AccuScan, Columbus, OH, USA) and allowed to explore for 30 min testing
477 period. Locomotor activity was automatically analyzed using AccuScan Fusion software (Omnitech).
478 Parameters included total distance traveled and mean motor speed.

479 **Rotarod**: This assay was performed as described previously (Coffin et al. 2023). Mice (9-11 weeks of
480 age) were placed on a rotating rod (3 cm diameter, 30 cm length; Ugo Basile) and tested for four
481 consecutive days, with four trials per day and a minimum 30-min inter-trial interval. Each trial lasted a
482 maximum of 10 min. The rod accelerated linearly from 5 to 40 rpm over the first 5 min, and then
483 remained at 40 rpm for the final 5 min. Latency to fall was recorded, with two consecutive passive
484 rotations scored as a fall.

485 **Conditioned fear**: On day 1, mice (19-21 weeks of age) were placed in a conditioning chamber
486 (Actimetrics, Coulbourn instruments, Wilmette, IL) and presented with two conditioned stimulus (CS)-
487 unconditioned stimulus (US) pairings, programmed using the FreezeFrame software (Actimetrics). The
488 trial comprised of 2 min of no sound, followed by 30 s of sound at 80 dB (CS), which was followed by a
489 mild 0.8 mA foot shock for 2 s (US). The tone-shock pairing was repeated after 2 minutes. Twenty-four
490 hours later, contextual memory was assessed by returning the mice to the same chamber for 5 min and
491 quantifying freezing behavior. One hour later, cued fear memory was assessed in a novel chamber by
492 monitoring freezing for 3 min without stimulus, followed by 3 min with the tone. Freezing was recorded
493 and quantified using FreezeFrame software (Actimetrics).

494

495 **Protein extraction for size exclusion chromatography**

496 Cortical or cerebellar tissues were collected from two 2–3-month-old mice per genotype and pooled per
497 biological replicate. Tissues were homogenized in TX buffer (50 mM Tris, pH 8.0; 75 mM NaCl; 0.5%
498 Triton X-100; Sigma) supplemented with freshly added protease inhibitor (GenDEPOT, P3100-020) and
499 phosphatase inhibitors (GenDEPOT, P3200-020) using a Dounce homogenizer. Homogenates were
500 extracted at 4 °C for 20 min with rotation and clarified by centrifugation at 20,000 × g for 10 min.
501 Supernatants were re-centrifuged, filtered through 0.45 μm centrifugal filters (Millipore), and protein
502 concentrations were determined by BCA assay (Pierce).

503

504 **Size exclusion chromatography**

505 Gel filtration chromatography was performed on a Superose 6 10/300 GL column (Cytiva) using an
506 AKTA Pure system at 4 °C. The column was equilibrated in 50 mM Tris (pH 8.0), 50 mM NaCl, 0.1%
507 Triton X-100. Column calibration was performed with thyroglobulin (667 kDa), apoferritin (440 kDa),
508 alcohol dehydrogenase (150 kDa), BSA (66 kDa), and cytochrome C (14.3 kDa). Fractions (1 mL) were
509 collected, supplemented with protease inhibitor (GenDEPOT, P3100-020) and phosphatase inhibitors
510 (GenDEPOT, P3200-020), and analyzed by SDS-PAGE on NuPAGE 3–8% Tris-Acetate gels
511 (Invitrogen).

512

513 **Cloning**

514 The hCIC-S cDNA was obtained from a previously described plasmid (Lam et al. 2006). The unique N-
515 terminal region of hCIC-L was synthesized (GenScript) and cloned into a PU57 backbone. Because
516 direct amplification of the ~4.8 kb CIC-Shared region was hindered by high GC content at the 3′ end, a
517 two-step cloning strategy was employed: the 5′ and 3′ CIC fragments were first assembled into
518 pENTR223 containing a synthetic multiple cloning site with an AvrII site, followed by insertion of the
519 ~4 kb central CIC fragment by PCR to generate full-length CIC-Shared.

520 A W37A point mutation (W37A in CIC-S, corresponding to W946A in CIC-L) was introduced into
521 hCIC-Shared in pENTR223 using gene blocks and Gibson assembly (New England Biolabs (NEB),
522 E2621L) after XhoI (5′ end) and StuI (N-terminal) digestion. CIC-L and CIC-S entry clones were
523 generated by Gibson assembly of the respective unique 5′ regions into the CIC-Shared backbone,
524 followed by addition of C-terminal V5 tags. The hCIC-L–unique sequence was cloned into pENTR223
525 with an N-terminal V5 tag and a stop codon after amino acid 931. All entry clones were recombined into
526 pcDNA3.1-DEST (derived from pcDNA3.1-3×FLAG-DEST, with stop codons preventing FLAG
527 expression) using Gateway LR recombination (Thermo Fisher).

528 The hATXN1L cDNA (Horizon Discovery) was cloned with an added N-terminal FLAG tag into pLV-
529 EF1α-IRES-Puro (Hayer et al. 2016) using PCR amplification and Gibson assembly. The FLAG-
530 hATXN1 coding sequence was obtained from the previously described pcDNA1-ATXN1 plasmid (Kim
531 et al. 2013) and cloned into pcDNA3.1 by Gibson assembly.

532

533 **Transfection and co-immunoprecipitation in HEK293T cells**

534 HEK293T cells were transfected with the indicated plasmids using TransIT-293 transfection reagent
535 (Mirus Bio) according to the manufacturer's instructions and incubated for 48–72 h. Cells were washed

536 with PBS and either processed immediately or stored at –80 °C. Frozen cells were thawed on ice and
537 lysed in cold lysis buffer (75 mM NaCl, 5 mM $MgCl_2$, 50 mM Tris-HCl (pH 8.0), 0.5% Triton X-100,
538 with protease and phosphatase inhibitors) for 30–60 min at 4 °C with rotation. Lysates were cleared by
539 centrifugation at 20,000 × g for 20 min at 4 °C.

540 For co-immunoprecipitation, lysates from one well of a 6-well plate were incubated with 1 µg V5
541 antibody (Invitrogen) pre-bound to 15 µL Protein G Dynabeads (Fisher Scientific, Cat. #10-009-D) for
542 2–4 h at 4 °C with rotation. Beads were washed four times with lysis buffer, and bound proteins were
543 eluted in 1× NuPAGE Sample Reducing Agent and NuPAGE LDS Sample Buffer (Invitrogen), boiled
544 for 10 min, and analyzed by SDS-PAGE on NuPAGE 3–8% Tris-Acetate gels (Invitrogen).

545

546 **Immunoprecipitation in mouse brain tissue**

547 Cortices from 12-week-old WT mice were homogenized in either cold NEMT buffer (50 mM Tris-HCl
548 pH 7.5, 150 mM NaCl, 1 mM EDTA, 0.5% NP-40) or lysis buffer (75 mM NaCl, 5 mM $MgCl_2$, 50 mM
549 Tris-HCl pH 8.0, 0.5% Triton X-100), each supplemented with freshly added protease inhibitor
550 (GenDEPOT, P3100-020) and phosphatase inhibitors (GenDEPOT, P3200-020). Tissue homogenization
551 was performed using an electric pestle (handheld polytron, WPR, 47747-370), followed by mechanical
552 shearing through a 27G syringe. Lysates were incubated on ice for 20 min and clarified by centrifugation
553 at 20,000 × g for 20 min at 4 °C. Ten percent of the supernatant was reserved as input, and the remaining
554 lysate was precleared with Dynabeads Protein G (Fisher Scientific, 10-009-D) for 30 min at 4 °C.
555 Precleared lysates were incubated for 2–3 h at 4 °C with 1–2 µg of antibody—anti-ATXN1 (534, in-
556 house (Gennarino et al. 2018)), anti-ATXN1L (881, in-house), or mouse IgG control—conjugated to 30
557 µL Dynabeads Protein G. Beads were washed four times with the corresponding lysis buffer and final

558 wash with PBS. Bound proteins were eluted in 1× NuPAGE Sample Reducing Agent and NuPAGE LDS
559 Sample Buffer (Invitrogen), boiled for 10 min, and analyzed by SDS-PAGE on NuPAGE 3–8% Tris-
560 Acetate gels (Invitrogen).

561 For *Atxn1*-KO experiments, cortex, hippocampus, cerebellum, and brainstem were dissected from 4-
562 week-old WT and *Atxn1*-KO mice and processed using the ATXN1 immunoprecipitation protocol
563 described above.

564

565 **Protein extraction for immunoblotting**

566 Brain and lung tissues were collected at postnatal day zero (P0), P6, P21, and 12 weeks and snap-frozen
567 in liquid nitrogen and kept in -80°C until processing. For protein extraction, frozen tissues were
568 homogenized in cold lysis buffer (75 mM NaCl, 5 mM $MgCl_2$, 50 mM Tris pH 8.0, 0.5% Triton X-100,
569 supplemented with freshly added protease inhibitor (GenDEPOT, P3100-020) and phosphatase
570 inhibitors (GenDEPOT, P3200-020) using an electric pestle (handheld polytron, WPR, 47747-370),
571 followed by mechanical shearing through a 27G syringe. Lysates were incubated on ice for 20 min and
572 centrifuged at 20,000 × g for 20 min at 4 °C. Protein concentrations in the supernatant were measured
573 using the Pierce BCA Protein Assay Kit (Thermo Fisher Scientific), and samples were normalized to
574 equal concentrations.

575

576 **Western blot analysis**

577 For immunoblotting, samples were mixed with NuPAGE Sample Reducing Agent and NuPAGE LDS
578 Sample Buffer (Invitrogen), boiled for 10 min, and run on NuPAGE 3–8% Tris-Acetate gels

579 (Invitrogen). Proteins were transferred to nitrocellulose membranes (Amersham, #10600004) using
580 transfer buffer containing 10% methanol. Membranes were blocked with either 5% skim milk in Tris-
581 buffered saline with 0.1% Tween® 20 (TBST) or Intercept (TBS) Blocking Buffer (LI-COR
582 Biosciences) for 1 h at room temperature and incubated overnight at 4 °C with primary antibodies
583 diluted in 3% BSA in TBST. The following primary antibodies were used: anti-CIC (rabbit, in-house,
584 1:1,000), anti-ATXN1(Servadio et al. 1995) (rabbit, in-house, 11750VII, 1:2,000), anti-ATXN1L
585 (mouse, 674, in-house, 1:1,000), anti-Vinculin (mouse, Sigma-Aldrich, 1:5,000), anti-Flag (Sigma-
586 Aldrich, 1:4000), and anti-V5 (Invitrogen, 1:2,000).

587 After washing in TBST, membranes were incubated for 1 h at room temperature with either HRP-
588 conjugated secondary antibodies (Jackson ImmunoResearch, 1:10,000 in 5% milk/TBST) or
589 fluorophore-conjugated secondary antibodies (LI-COR Biosciences, 1:10,000 in Intercept Blocking
590 Buffer). HRP blots were developed using ECL (Cytiva, RPN2236) or SuperSignal Femto (Thermo
591 Fisher Scientific, 34095) and imaged with a GE Amersham Imager 680 or ChemiDoc MP Imaging
592 System or LI-COR Odyssey M system. Fluorescent blots were imaged directly using the LI-COR
593 Odyssey M system.

594

595 **Statistical analysis**

596 All statistical analyses were performed using GraphPad Prism 9.0, except for RNA-seq analyses.
597 Survival of animals was compared to the expected Mendelian ratio using a chi-square test. Comparisons
598 between two groups were performed using unpaired t-tests. Comparisons involving more than two
599 groups were analyzed by one-way or two-way ANOVA with appropriate post hoc multiple-comparisons
600 tests. Repeated-measures data were analyzed by two-way repeated-measures ANOVA. Survival curves

601 were analyzed using the Mantel–Cox test. Specific statistical tests are indicated in the figure legends.
602 Data are presented as mean ± SEM. In each case, *, **, ***, **** and ns denote $p<0.05$, $p<0.01$,
603 $p<0.001$, $p<0.0001$ and $p>0.05$, respectively.

604 RNA-seq analyses were performed in R using DESeq2, as described in the supplementary methods.
605 Fisher's exact test was used to calculate odds ratios and p-values for gene set overlaps.

606 Sample sizes were based on prior studies and standard practice in the field. Biological replicates refer to
607 independent animals. Experimental analyses were performed in a blinded manner whenever possible.

608

609 **Data and material availability**

610 All data needed to evaluate the conclusions in this study are present in here and/or the in the
611 Supplemental Material. RNA sequencing reads and processed data were deposited to GEO
612 (GSE310453).

613

614 **COMPETING INTEREST STATEMENT**

615 The authors declare no competing interests.

616

617 **ACKNOWLEDGEMENTS**

618 We thank Ji-Yoen Kim, Sameer Bajikar, Dah-eun Chloe Chung, Harini Pallikarana, Sih-Rong Wu, and
619 Xue Deng for their critical comments on the manuscript, and Harry Orr and Vicky Brandt for editorial
620 input. We thank Zhijian Yu for technical support in bioinformatics analyses during manuscript revisions.

621 We further thank the Baylor College of Medicine (BCM) Genetically Engineered Rodent Model
622 (GERM) Core, Jan and Dan Duncan Neurological Research Institute (NRI) Rodent Neurobehavior Core,
623 and Neuropathology Core. Funding: This work was funded by National Institute of Aging F31
624 AG077918 (H.L.), Cockrell Family Funding (H.L.), National Institute of Neurological Disorders and
625 Stroke R01 NS027699 (H.Y.Z.), Freedom Together Foundation MR-2023-4260 (H.Y.Z.), Howard
626 Hughes Medical Institute (H.Y.Z.), National Heart, Lung, and Blood Institute R01 HL181470 (B.S.),
627 Chao Endowment (Z.L.), Huffington Foundation (Z.L.), National Institutes of Health Cancer Center P30
628 CA125123 (BCM GERM Core), Cancer Biology Research 1R50CA283804 (BCM GERM Core),
629 Eunice Kennedy Shriver National Institute of Child Health and Human Development Intellectual and
630 Developmental Disabilities Research Center P50HD103555 (NRI Rodent Neurobehavior Core and
631 Neovascularization Core).

632 *Author contributions:* H.L. and H.Y.Z. conceived the study, designed the experiments, and analyzed and
633 interpreted the data. H.L. generated mouse models. H.L., E.V.G., and E.M.R. performed protein
634 biochemistry from mouse tissues, and H.L. performed cellular experiments. H.L. and E.H.-Y.C.
635 performed RNA extractions, and H.C. performed alignment of raw sequencing data; H.L. performed
636 RNA-seq analysis. H.C. and Z.L. supervised RNA-seq processing and analysis. H.L., E.H.-Y.C., and
637 K.X. performed mouse genotyping, colony management, and survival and weight tracking. M.A.D.
638 designed and generated the hCIC-L plasmid. H.L. and M.A.D. generated mutant constructs and
639 performed additional cloning, with technical assistance from E.H.-Y.C. R.R. performed size-exclusion
640 chromatography. S.V. performed mouse behavior experiments. B.S. processed lung tissue for
641 histopathology and performed morphometric analysis. H.L. wrote the manuscript and prepared the
642 figures with input from all authors. H.Y.Z. reviewed all data and edited the manuscript.

643

644 **REFERENCES**

645 Ahmad ST, Rogers AD, Chen MJ, Dixit R, Adnani L, Frankiw LS, Lawn SO, Blough MD, Alshehri M,
646 Wu W et al. 2019. Capicua regulates neural stem cell proliferation and lineage specification
647 through control of Ets factors. *Nat Commun* **10**: 2000.
648 Asher M, Rosa JG, Rainwater O, Duvick L, Bennyworth M, Lai RY, Crc SCA, Kuo SH, Cvetanovic M.
649 2020. Cerebellar contribution to the cognitive alterations in SCA1: evidence from mouse models.
650 *Hum Mol Genet* **29**: 117-131.
651 Banfi S, Servadio A, Chung MY, Kwiatkowski TJ, Jr., McCall AE, Duvick LA, Shen Y, Roth EJ, Orr
652 HT, Zoghbi HY. 1994. Identification and characterization of the gene causing type 1
653 spinocerebellar ataxia. *Nat Genet* **7**: 513-520.
654 Bertram L, Lange C, Mullin K, Parkinson M, Hsiao M, Hogan MF, Schjeide BM, Hooli B, Divito J,
655 Ionita I et al. 2008. Genome-wide association analysis reveals putative Alzheimer's disease
656 susceptibility loci in addition to APOE. *Am J Hum Genet* **83**: 623-632.
657 Bettens K, Brouwers N, Van Miegroet H, Gil A, Engelborghs S, De Deyn PP, Vandenberghe R, Van
658 Broeckhoven C, Sleegers K. 2010. Follow-up study of susceptibility loci for Alzheimer's disease
659 and onset age identified by genome-wide association. *J Alzheimers Dis* **19**: 1169-1175.
660 Bowman AB, Lam YC, Jafar-Nejad P, Chen HK, Richman R, Samaco RC, Fryer JD, Kahle JJ, Orr HT,
661 Zoghbi HY. 2007. Duplication of Atxn1l suppresses SCA1 neuropathology by decreasing
662 incorporation of polyglutamine-expanded ataxin-1 into native complexes. *Nat Genet* **39**: 373-
663 379.
664 Chen HK, Fernandez-Funez P, Acevedo SF, Lam YC, Kaytor MD, Fernandez MH, Aitken A, Skoulakis
665 EM, Orr HT, Botas J et al. 2003. Interaction of Akt-phosphorylated ataxin-1 with 14-3-3
666 mediates neurodegeneration in spinocerebellar ataxia type 1. *Cell* **113**: 457-468.
667 Chung DC, Roemer S, Petrucelli L, Dickson DW. 2021. Cellular and pathological heterogeneity of
668 primary tauopathies. *Mol Neurodegener* **16**: 57.
669 Coffin SL, Durham MA, Nitschke L, Xhako E, Brown AM, Revelli JP, Villavicencio Gonzalez E, Lin T,
670 Handler HP, Dai Y et al. 2023. Disruption of the ATXN1-CIC complex reveals the role of
671 additional nuclear ATXN1 interactors in spinocerebellar ataxia type 1. *Neuron* **111**: 481-492
672 e488.
673 Crespo-Barreto J, Fryer JD, Shaw CA, Orr HT, Zoghbi HY. 2010. Partial loss of ataxin-1 function
674 contributes to transcriptional dysregulation in spinocerebellar ataxia type 1 pathogenesis. *PLoS*
675 *Genet* **6**: e1001021.
676 Dissanayake K, Toth R, Blakey J, Olsson O, Campbell DG, Prescott AR, MacKintosh C. 2011.
677 ERK/p90(RSK)/14-3-3 signalling has an impact on expression of PEA3 Ets transcription factors
678 via the transcriptional repressor capicua. *Biochem J* **433**: 515-525.
679 Fores M, Ajuria L, Samper N, Astigarraga S, Nieva C, Grossman R, Gonzalez-Crespo S, Paroush Z,
680 Jimenez G. 2015. Origins of context-dependent gene repression by capicua. *PLoS Genet* **11**:
681 e1004902.
682 Friedrich J, Kordasiewicz HB, O'Callaghan B, Handler HP, Wagener C, Duvick L, Swayze EE,
683 Rainwater O, Hofstra B, Benneyworth M et al. 2018. Antisense oligonucleotide-mediated ataxin-
684 1 reduction prolongs survival in SCA1 mice and reveals disease-associated transcriptome
685 profiles. *JCI Insight* **3**.
686 Fryer JD, Yu P, Kang H, Mandel-Brehm C, Carter AN, Crespo-Barreto J, Gao Y, Flora A, Shaw C, Orr
687 HT et al. 2011. Exercise and genetic rescue of SCA1 via the transcriptional repressor Capicua.
688 *Science* **334**: 690-693.

689 Fu H, Hardy J, Duff KE, Fu H, Hardy J, Duff KE. 2018. Selective vulnerability in neurodegenerative
690 diseases. *Nature Neuroscience 2018 21:10* **21**.
691 Gennarino VA, Palmer EE, McDonell LM, Wang L, Adamski CJ, Koire A, See L, Chen CA, Schaaf CP,
692 Rosenfeld JA et al. 2018. A Mild PUM1 Mutation Is Associated with Adult-Onset Ataxia,
693 whereas Haploinsufficiency Causes Developmental Delay and Seizures. *Cell* **172**: 924-936 e911.
694 Hayer A, Shao L, Chung M, Joubert LM, Yang HW, Tsai FC, Bisaria A, Betzig E, Meyer T. 2016.
695 Engulfed cadherin fingers are polarized junctional structures between collectively migrating
696 endothelial cells. *Nat Cell Biol* **18**: 1311-1323.
697 Hwang I, Pan H, Yao J, Elemento O, Zheng H, Paik J. 2020. CIC is a critical regulator of neuronal
698 differentiation. *JCI Insight* **5**.
699 Jafar-Nejad P, Ward CS, Richman R, Orr HT, Zoghbi HY. 2011. Regional rescue of spinocerebellar
700 ataxia type 1 phenotypes by 14-3-3epsilon haploinsufficiency in mice underscores complex
701 pathogenicity in neurodegeneration. *Proc Natl Acad Sci U S A* **108**: 2142-2147.
702 Jimenez G, Shvartsman SY, Paroush Z. 2012. The Capicua repressor--a general sensor of RTK signaling
703 in development and disease. *J Cell Sci* **125**: 1383-1391.
704 Kampmann M. 2024. Molecular and cellular mechanisms of selective vulnerability in neurodegenerative
705 diseases. *Nat Rev Neurosci* **25**: 351-371.
706 Kang J, Lemaire HG, Unterbeck A, Salbaum JM, Masters CL, Grzeschik KH, Multhaup G, Beyreuther
707 K, Müller-Hill B. 1987. The precursor of Alzheimer's disease amyloid A4 protein resembles a
708 cell-surface receptor. *Nature* **325**: 733-736.
709 Kim E, Lu HC, Zoghbi HY, Song JJ. 2013. Structural basis of protein complex formation and
710 reconfiguration by polyglutamine disease protein Ataxin-1 and Capicua. *Genes Dev* **27**: 590-595.
711 Kim E, Park S, Choi N, Lee J, Yoe J, Kim S, Jung HY, Kim KT, Kang H, Fryer JD et al. 2015.
712 Deficiency of Capicua disrupts bile acid homeostasis. *Sci Rep* **5**: 8272.
713 Kitaguchi N, Takahashi Y, Tokushima Y, Shiojiri S, Ito H. 1988. Novel precursor of Alzheimer's disease
714 amyloid protein shows protease inhibitory activity. *Nature* **331**: 530-532.
715 Kjer-Hansen P, Phan TG, Weatheritt RJ. 2024. Protein isoform-centric therapeutics: expanding targets
716 and increasing specificity. *Nat Rev Drug Discov* **23**: 759-779.
717 Kozareva V, Martin C, Osorno T, Rudolph S, Guo C, Vanderburg C, Nadaf N, Regev A, Regehr WG,
718 Macosko E. 2021. A transcriptomic atlas of mouse cerebellar cortex comprehensively defines
719 cell types. *Nature* **598**: 214-219.
720 Lam YC, Bowman AB, Jafar-Nejad P, Lim J, Richman R, Fryer JD, Hyun ED, Duvick LA, Orr HT,
721 Botas J et al. 2006. ATAXIN-1 interacts with the repressor Capicua in its native complex to cause
722 SCA1 neuropathology. *Cell* **127**: 1335-1347.
723 Lee Y. 2020. Regulation and function of capicua in mammals. *Exp Mol Med* **52**: 531-537.
724 Lee Y, Fryer JD, Kang H, Crespo-Barreto J, Bowman AB, Gao Y, Kahle JJ, Hong JS, Kheradmand F,
725 Orr HT et al. 2011. ATXN1 protein family and CIC regulate extracellular matrix remodeling and
726 lung alveolarization. *Dev Cell* **21**: 746-757.
727 Lim J, Crespo-Barreto J, Jafar-Nejad P, Bowman AB, Richman R, Hill DE, Orr HT, Zoghbi HY. 2008.
728 Opposing effects of polyglutamine expansion on native protein complexes contribute to SCA1.
729 *Nature* **452**: 713-718.
730 Lu HC, Tan Q, Rousseaux MW, Wang W, Kim JY, Richman R, Wan YW, Yeh SY, Patel JM, Liu X et al.
731 2017. Disruption of the ATXN1-CIC complex causes a spectrum of neurobehavioral phenotypes
732 in mice and humans. *Nat Genet* **49**: 527-536.

733 Matilla A, Roberson ED, Banfi S, Morales J, Armstrong DL, Burright EN, Orr HT, Sweatt JD, Zoghbi
734 HY, Matzuk MM. 1998. Mice lacking ataxin-1 display learning deficits and decreased
735 hippocampal paired-pulse facilitation. *J Neurosci* **18**: 5508-5516.
736 Mizutani A, Wang L, Rajan H, Vig PJ, Alaynick WA, Thaler JP, Tsai CC. 2005. Boat, an AXH domain
737 protein, suppresses the cytotoxicity of mutant ataxin-1. *EMBO J* **24**: 3339-3351.
738 Orr HT, Chung MY, Banfi S, Kwiatkowski TJ, Jr., Servadio A, Beaudet AL, McCall AE, Duvick LA,
739 Ranum LP, Zoghbi HY. 1993. Expansion of an unstable trinucleotide CAG repeat in
740 spinocerebellar ataxia type 1. *Nat Genet* **4**: 221-226.
741 Ponte P, Gonzalez-DeWhitt P, Schilling J, Miller J, Hsu D, Greenberg B, Davis K, Wallace W,
742 Lieberburg I, Fuller F. 1988. A new A4 amyloid mRNA contains a domain homologous to serine
743 proteinase inhibitors. *Nature* **331**: 525-527.
744 Rhinn H, Qiang L, Yamashita T, Rhee D, Zolin A, Vanti W, Abeliovich A. 2012. Alternative α-synuclein
745 transcript usage as a convergent mechanism in Parkinson's disease pathology. *Nat Commun* **3**:
746 1084.
747 Rodriguez-Munoz L, Lagares C, Gonzalez-Crespo S, Castel P, Veraksa A, Jimenez G. 2022.
748 Noncanonical function of Capicua as a growth termination signal in Drosophila oogenesis. *Proc*
749 *Natl Acad Sci U S A* **119**: e2123467119.
750 Rousseaux MWC, Tschumperlin T, Lu HC, Lackey EP, Bondar VV, Wan YW, Tan Q, Adamski CJ,
751 Friedrich J, Twaroski K et al. 2018. ATXN1-CIC Complex Is the Primary Driver of Cerebellar
752 Pathology in Spinocerebellar Ataxia Type 1 through a Gain-of-Function Mechanism. *Neuron* **97**:
753 1235-1243 e1235.
754 Serra HG, Duvick L, Zu T, Carlson K, Stevens S, Jorgensen N, Lysholm A, Burright E, Zoghbi HY,
755 Clark HB et al. 2006. RORalpha-mediated Purkinje cell development determines disease severity
756 in adult SCA1 mice. *Cell* **127**: 697-708.
757 Servadio A, Koshy B, Armstrong D, Antalffy B, Orr HT, Zoghbi HY. 1995. Expression analysis of the
758 ataxin-1 protein in tissues from normal and spinocerebellar ataxia type 1 individuals. *Nat Genet*
759 **10**: 94-98.
760 Sharma S, Hourigan B, Patel Z, Rosenfeld JA, Chan KM, Wangler MF, Yi JS, Lehman A, Study C,
761 Horvath G et al. 2022. Novel CIC variants identified in individuals with neurodevelopmental
762 phenotypes. *Hum Mutat* **43**: 889-899.
763 Shrestha AK, Bettini ML, Menon RT, Gopal VYN, Huang S, Edwards DP, Pammi M, Barrios R,
764 Shivanna B. 2019. Consequences of early postnatal lipopolysaccharide exposure on developing
765 lungs in mice. *Am J Physiol Lung Cell Mol Physiol* **316**: L229-l244.
766 Simon-Carrasco L, Grana O, Salmon M, Jacob HKC, Gutierrez A, Jimenez G, Drosten M, Barbacid M.
767 2017. Inactivation of Capicua in adult mice causes T-cell lymphoblastic lymphoma. *Genes Dev*
768 **31**: 1456-1468.
769 Sprecher CA, Grant FJ, Grimm G, O'Hara PJ, Norris F, Norris K, Foster DC. 1993. Molecular cloning of
770 the cDNA for a human amyloid precursor protein homolog: evidence for a multigene family.
771 *Biochemistry* **32**: 4481-4486.
772 Subramanian A, Tamayo P, Mootha VK, Mukherjee S, Ebert BL, Gillette MA, Paulovich A, Pomeroy
773 SL, Golub TR, Lander ES et al. 2005. Gene set enrichment analysis: A knowledge-based
774 approach for interpreting genome-wide expression profiles. *Proceedings of the National*
775 *Academy of Sciences* **102**.
776 Suh J, Romano DM, Nitschke L, Herrick SP, DiMarzio BA, Dzhala V, Bae JS, Oram MK, Zheng Y,
777 Hooli B et al. 2019. Loss of Ataxin-1 Potentiates Alzheimer's Pathogenesis by Elevating Cerebral
778 BACE1 Transcription. *Cell* **178**: 1159-1175 e1117.

Swaminathan S, Kim S, Shen L, Risacher SL, Foroud T, Pankratz N, Potkin SG, Huentelman MJ, Craig DW, Weiner MW et al. 2011. Genomic Copy Number Analysis in Alzheimer's Disease and Mild Cognitive Impairment: An ADNI Study. *Int J Alzheimers Dis* **2011**: 729478.

Swaminathan S, Shen L, Kim S, Inlow M, West JD, Faber KM, Foroud T, Mayeux R, Saykin AJ, Alzheimer's Disease Neuroimaging I et al. 2012. Analysis of copy number variation in Alzheimer's disease: the NIALOAD/ NCRAD Family Study. *Curr Alzheimer Res* **9**: 801-814.

Tan Q, Zoghbi HY. 2019. Mouse models as a tool for discovering new neurological diseases. *Neurobiol Learn Mem* **165**: 106902.

Tanzi RE, McClatchey AI, Lamperti ED, Villa-Komaroff L, Gusella JF, Neve RL. 1988. Protease inhibitor domain encoded by an amyloid protein precursor mRNA associated with Alzheimer's disease. *Nature* **331**: 528-530.

Tsuda H, Jafar-Nejad H, Patel AJ, Sun Y, Chen HK, Rose MF, Venken KJ, Botas J, Orr HT, Bellen HJ et al. 2005. The AXH domain of Ataxin-1 mediates neurodegeneration through its interaction with Gfi-1/Senseless proteins. *Cell* **122**: 633-644.

Wang Y, Mandelkow E. 2016. Tau in physiology and pathology. *Nature Reviews Neuroscience* **17**: 22-35.

Wasco W, Bupp K, Magendantz M, Gusella JF, Tanzi RE, Solomon F. 1992. Identification of a mouse brain cDNA that encodes a protein related to the Alzheimer disease-associated amyloid beta protein precursor. *Proc Natl Acad Sci U S A* **89**: 10758-10762.

Wasco W, Gurubhagavatula S, Paradis MD, Romano DM, Sisodia SS, Hyman BT, Neve RL, Tanzi RE. 1993. Isolation and characterization of APLP2 encoding a homologue of the Alzheimer's associated amyloid beta protein precursor. *Nat Genet* **5**: 95-100.

Weissmann S, Cloos PA, Sidoli S, Jensen ON, Pollard S, Helin K. 2018. The Tumor Suppressor CIC Directly Regulates MAPK Pathway Genes via Histone Deacetylation. *Cancer Res* **78**: 4114-4125.

Wong D, Sogerer L, Lee SS, Wong V, Lum A, Levine AB, Marra MA, Yip S. 2020. TRIM25 promotes Capicua degradation independently of ERK in the absence of ATXN1L. *BMC Biol* **18**: 154.

Yang X, Coulombe-Huntington J, Kang S, Sheynkman GM, Hao T, Richardson A, Sun S, Yang F, Shen YA, Murray RR et al. 2016. Widespread Expansion of Protein Interaction Capabilities by Alternative Splicing. *Cell* **164**: 805-817.

Zoghbi HY, Orr HT. 1995. Spinocerebellar ataxia type 1. *Semin Cell Biol* **6**: 29-35.

811 **TABLES**

812 **Table 1. Number of surviving animals from *Cic*$^{S\text{-KO}/+}$ intercrosses at a given time point**

Genotype	Observed (%) at P0	Observed (%) at P6	Observed (%) at P21
Cic$^{+/+}$	22 (24.4 %)	32 (28.1 %)	31 (29.8%)
Cic$^{S\text{-KO}/+}$	50 (55.6 %)	65 (57.0 %)	64 (61.5%)
Cic$^{S\text{-KO}/S\text{-KO}}$	18 (20.0 %)	17 (14.9 %)	9 (8.6 %)
Total	90	114	104
Chi-square*	ns (0.26)	ns (0.18)	** (0.007)

813 *Chi-square analysis of the observed ratio compared to the expected Mendelian ratios (1:2:1). Each time

814 point is an independent cohort. (**) $p<0.01$

815

816 **Table 2. Number of surviving animals from *Cic*$^{L\text{-KO}/+}$ intercrosses at a given time point**

Genotype	Observed (%) at P0	Observed (%) at P6	Observed (%) at P21
Cic$^{+/+}$	22 (20.9 %)	18 (25.7 %)	28 (26.7 %)
Cic$^{L\text{-KO}/+}$	53 (50.5 %)	38 (54.3 %)	54 (51.4 %)
Cic$^{L\text{-KO}/L\text{-KO}}$	30 (28.6 %)	14 (20.0 %)	23 (21.9 %)
Total	105	70	105
Chi-square*	ns (0.53)	ns (0.86)	ns (0.74)

817 *Chi-square analysis of the observed ratio compared to the expected Mendelian ratios (1:2:1). Each time

818 point is an independent cohort.

819

820 **FIGURES**

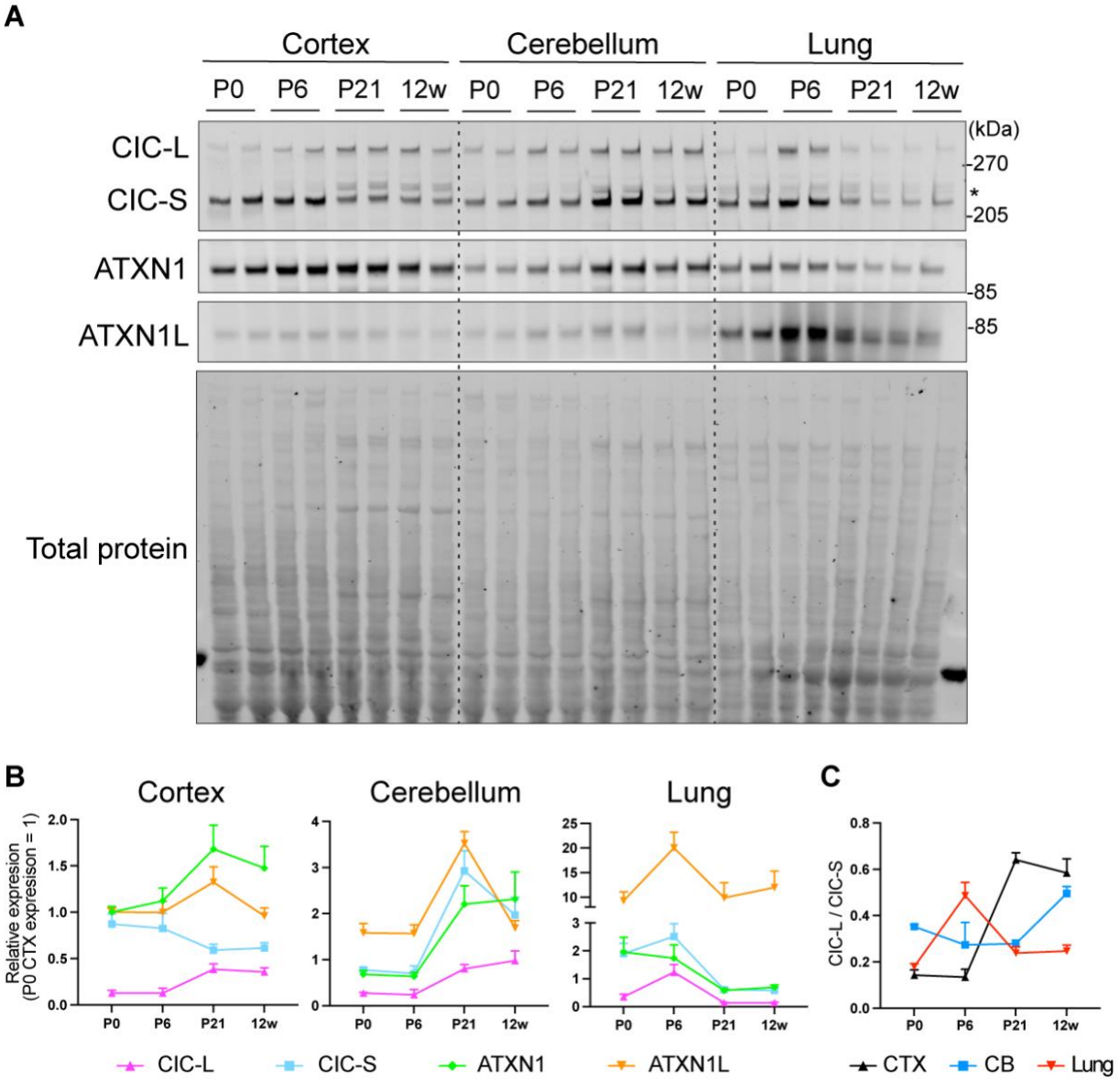

821

822

823 **Figure 1. CIC-L and CIC-S show different spatiotemporal expression patterns in mouse cortex,**
824 **cerebellum, and lung.**

825 (A) Representative immunoblot (IB) of CIC-L, CIC-S, ATXN1 and ATXN1L in wild-type (WT)
826 mouse cortex, cerebellum and lung lysates at indicated time points. Antibody against the C
827 terminus of CIC recognizes both isoforms of CIC. P, postnatal day; w: week-old; *, truncated
828 CIC-L product.
829 (B) Quantification of CIC-L, CIC-S, ATXN1, and ATXN1L protein levels. Each protein was
830 normalized to total protein, with each time point normalized to P0 cortex (CTX). CIC isoforms
831 were normalized to total CIC at P0 CTX. Data are mean ± SEM; n = 4 per time point.
832 (C) Ratio of CIC-L to CIC-S at each time point for each region. CTX, cortex; CB, cerebellum.

833

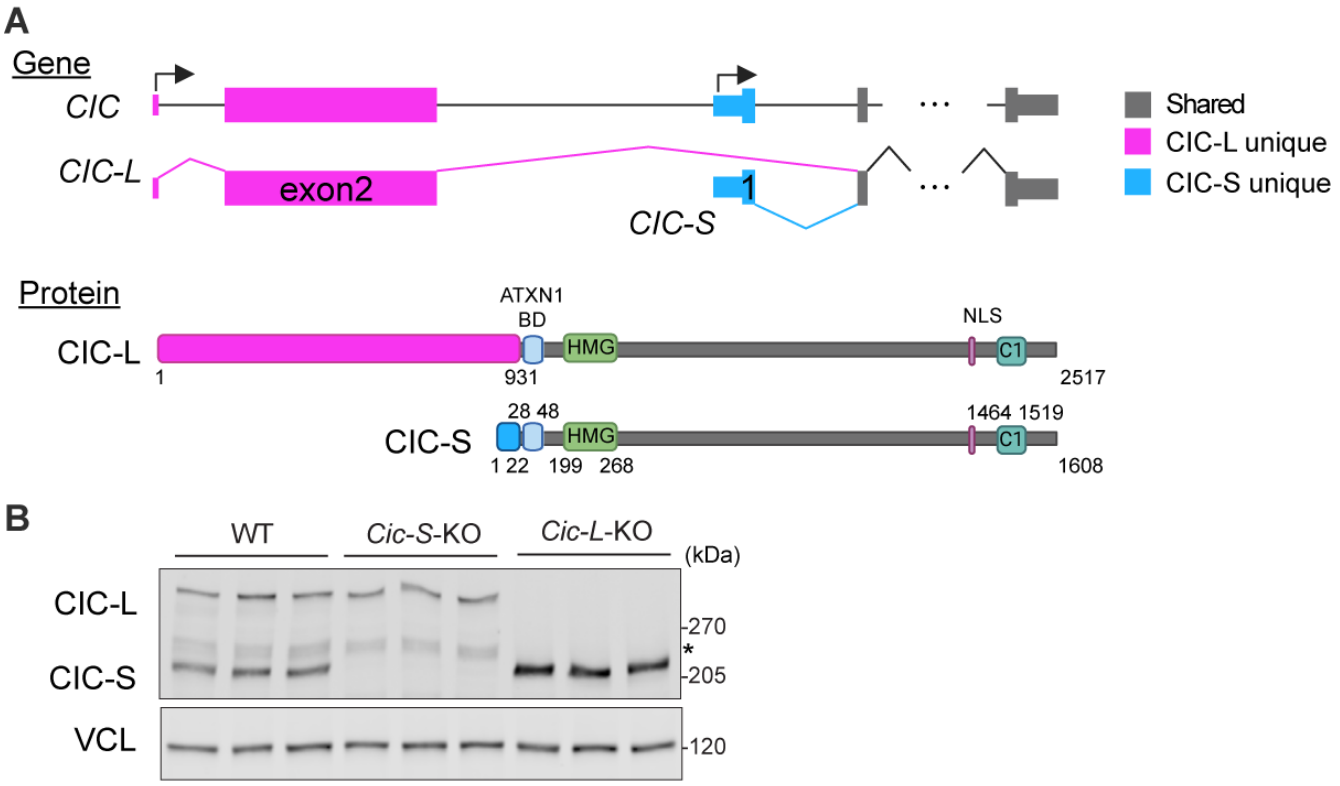

Figure 2. *Cic-L*-KO and *Cic-S*-KO mice were generated using CRISPR.

(A) Gene and protein structure of human CIC-L and CIC-S. ATXN1/1L BD, ATXN1/1L binding domain; HMG, HMG box; C1, C1 domain; NLS: Nuclear localization signal (Created in BioRender, https://BioRender.com/kjq2awu).

(B) IB of CIC-L and CIC-S of cortex lysate of WT, *Cic-S*-KO and *Cic-L*-KO mice at 1 month of age. Vinculin (VCL) as loading control. n =3 per genotype. *, truncated CIC-L product.

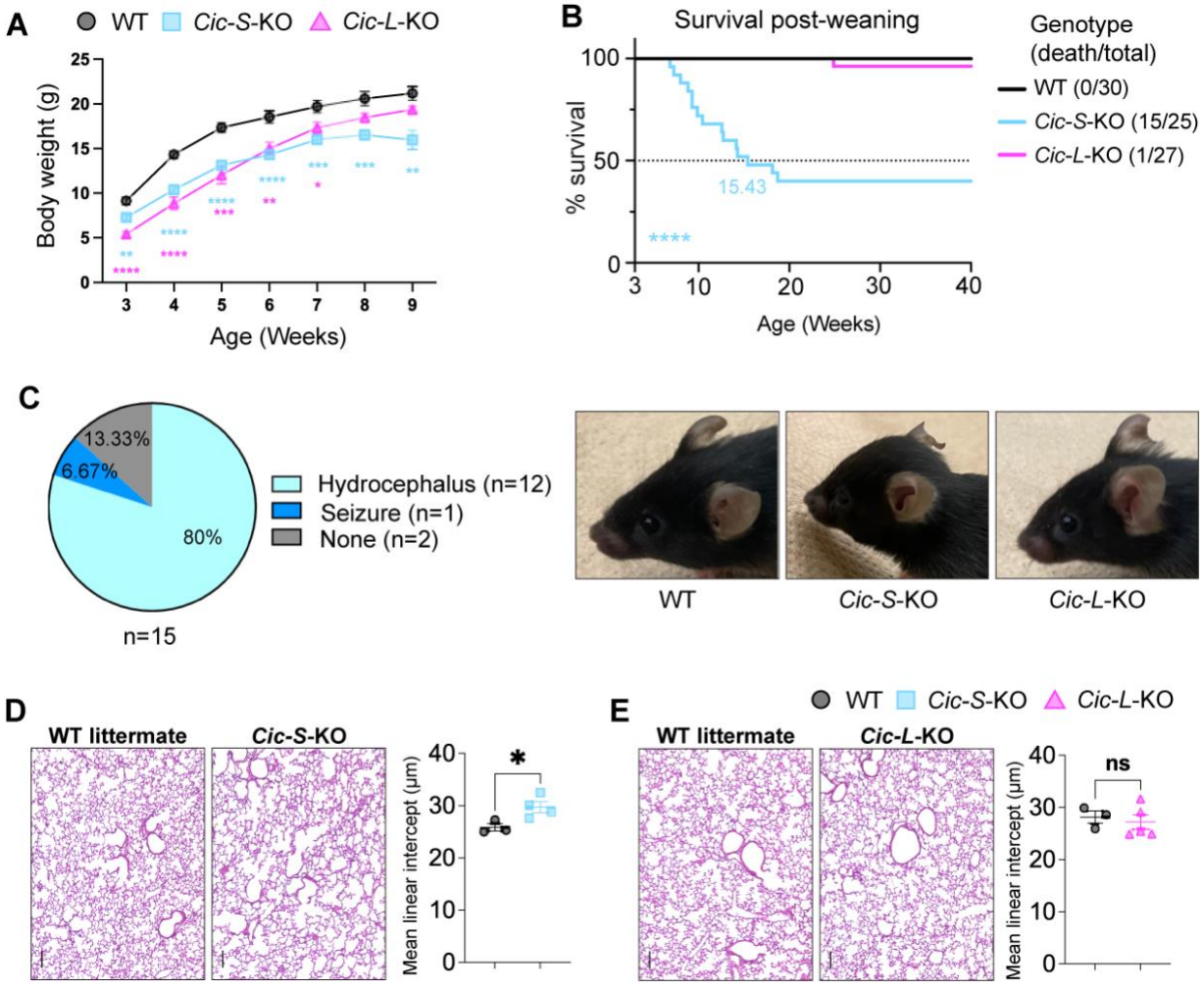
A
WT
Cic-S-KO
Cic-L-KO
Body weight (g)
Age (Weeks)
B
Survival post-weaning
% survival
Age (Weeks)
15.43
Genotype (death/total)
WT (0/30)
Cic-S-KO (15/25)
Cic-L-KO (1/27)
C
13.33%
6.67%
80%
Hydrocephalus (n=12)
Seizure (n=1)
None (n=2)
n=15
WT
Cic-S-KO
Cic-L-KO
D
WT littermate
Cic-S-KO
Mean linear intercept (µm)
E
WT littermate
Cic-L-KO
ns

842

843

844 **Figure 3. *Cic-S*-KO mice display early lethality and lung alveolarization defects.**

845 (A) Weekly body weights of *Cic-S*-KO, *Cic-L*-KO, and their WT littermate from week 3. Data are
846 mean ± SEM; n = 16 per genotype (8 males, 8 females). Two-way repeated-measures ANOVA
847 with Dunnett's multiple comparisons; (*) $p < 0.05$, (**) $p < 0.01$, (***) $p < 0.001$, (****) $p <$
848 0.0001.

849 (B) Kaplan–Meier survival curves post-weaning (3 weeks) for WT, *Cic-S*-KO, and *Cic-L*-KO mice
850 (n = 30, 25, and 27). Mantel–Cox test; (****) $p < 0.0001$.

851 (C) Left: Phenotypes observed before lethality of *Cic-S*-KO animals (n = 15). Right: Representative
852 photographs of the heads of WT, *Cic-S*-KO and *Cic-L*-KO mice at 9 weeks; *Cic-S*-KO mice
853 show dome-shaped heads due to hydrocephalus.

854 (D,E) Lung tissues from *Cic-S*-KO (D) and *Cic-L*-KO (E) mice and their WT littermates collected at
855 P21. Left: Representative hematoxylin and eosin (H&E)-stained lung sections. Scale bar,
856 100 μm. Right: Quantification of alveolar airspace by mean linear intercept (MLI). Data are
857 mean ± SEM; n = 3–5 per group. Unpaired t-test; (*) $p < 0.05$, (ns) $p > 0.05$.

858

859

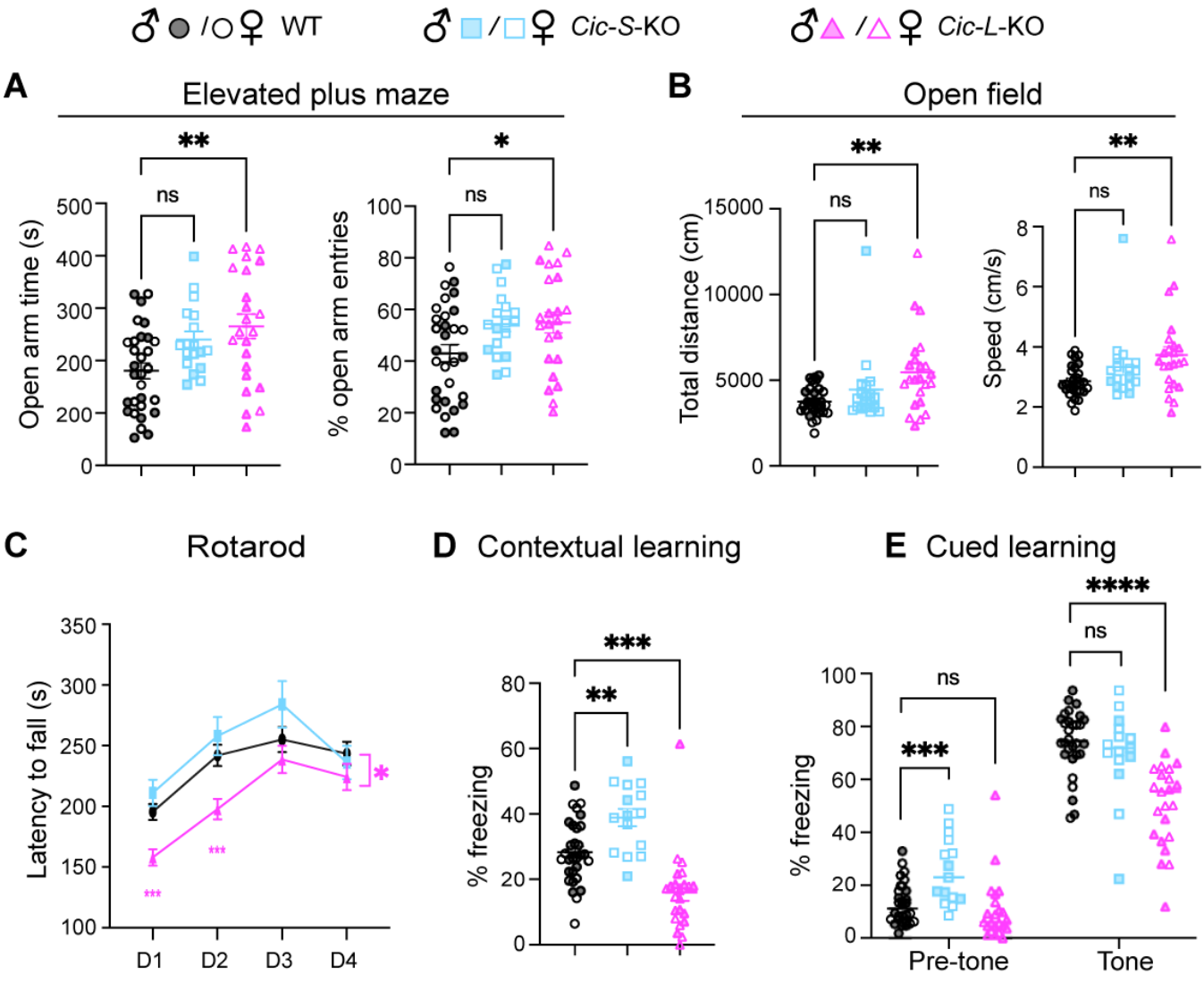
♂ ● / ○ ♀ WT
♂ ■ / □ ♀ Cic-S-KO
♂ ▲ / △ ♀ Cic-L-KO
A
Elevated plus maze
Open arm time (s)
% open arm entries
ns
**
*
B
Open field
Total distance (cm)
Speed (cm/s)
C
Rotarod
Latency to fall (s)
D1
D2
D3
D4
D
Contextual learning
% freezing
E
Cued learning
Pre-tone
Tone
****

861 **Figure 4. *Cic-L*-KO mice display neurobehavioral deficits.**

862 (A-E) Behavior characterization of *Cic-S*-KO, *Cic-L*-KO, and their WT littermate controls.

863 (A) Anxiety-like behavior measured using an elevated plus maze.

864 (B) Activity measured with open field assay.

865 (C) Motor coordination measured with rotarod. D, day; males and females combined.

866 (D,E) Learning and memory assessed with fear conditioning assay.

867 For (A,B), n = 30 WT (14 males, 16 females), n = 18 *Cic-S*-KO (5 males, 13 females), and n =
868 23 *Cic-L*-KO (12 males, 11 females). Due to early lethality of *Cic-S*-KO mice, n = 17 (5 males,
869 12 females) and n = 15 (4 males, 11 females) *Cic-S*-KO mice were analyzed for (C) and (D,E),
870 respectively. One-way ANOVA with Dunnett's multiple comparisons for (A,B,D,E); two-way
871 repeated-measures ANOVA with Dunnett's multiple comparisons for (C). Data are mean ± SEM;
872 (*) $p < 0.05$, (**) $p < 0.01$, (***) $p < 0.001$, (****) $p < 0.0001$, (ns) $p > 0.05$.

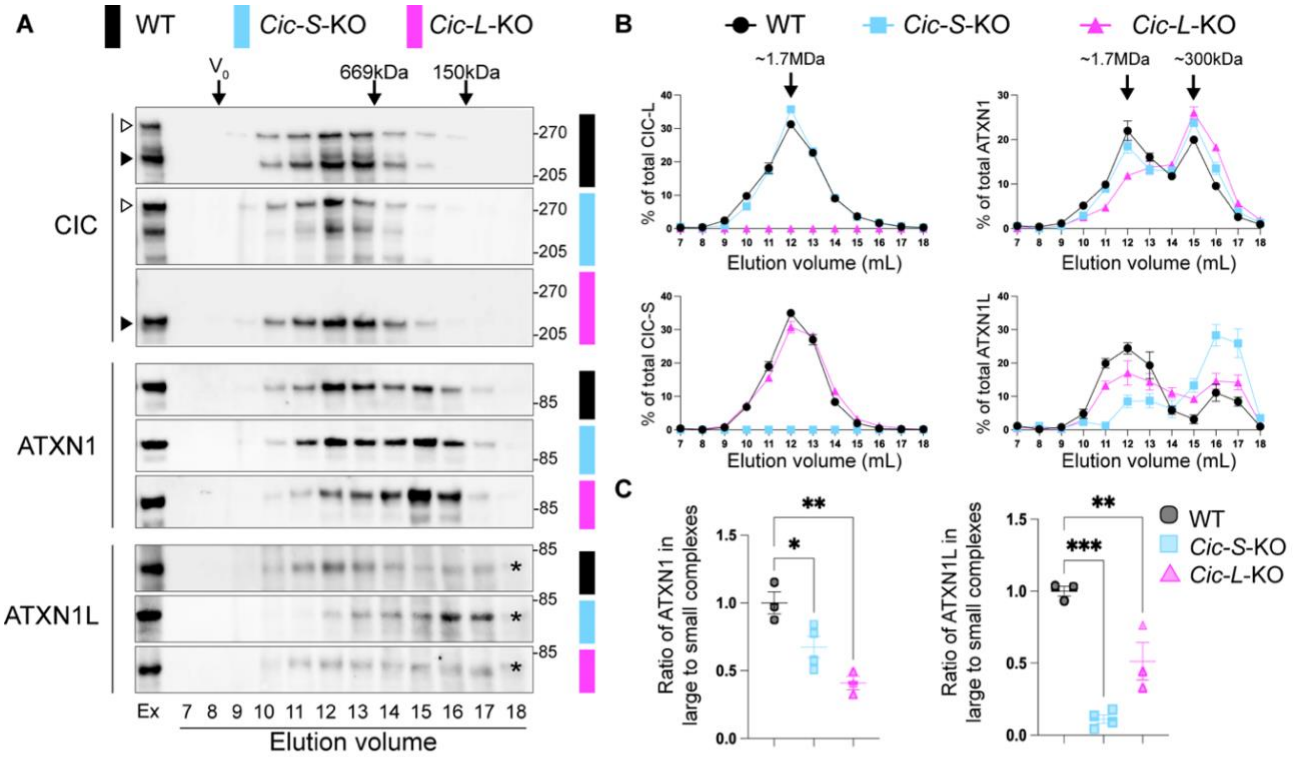
A
WT
Cic-S-KO
Cic-L-KO
V0
669kDa
150kDa
CIC
ATXN1
ATXN1L
-270
-205
-85
Ex 7 8 9 10 11 12 13 14 15 16 17 18
Elution volume
B
~1.7MDa
~300kDa
% of total CIC-L
% of total ATXN1
% of total CIC-S
% of total ATXN1L
Elution volume (mL)
C
Ratio of ATXN1 in large to small complexes
Ratio of ATXN1L in large to small complexes
WT
Cic-S-KO
Cic-L-KO

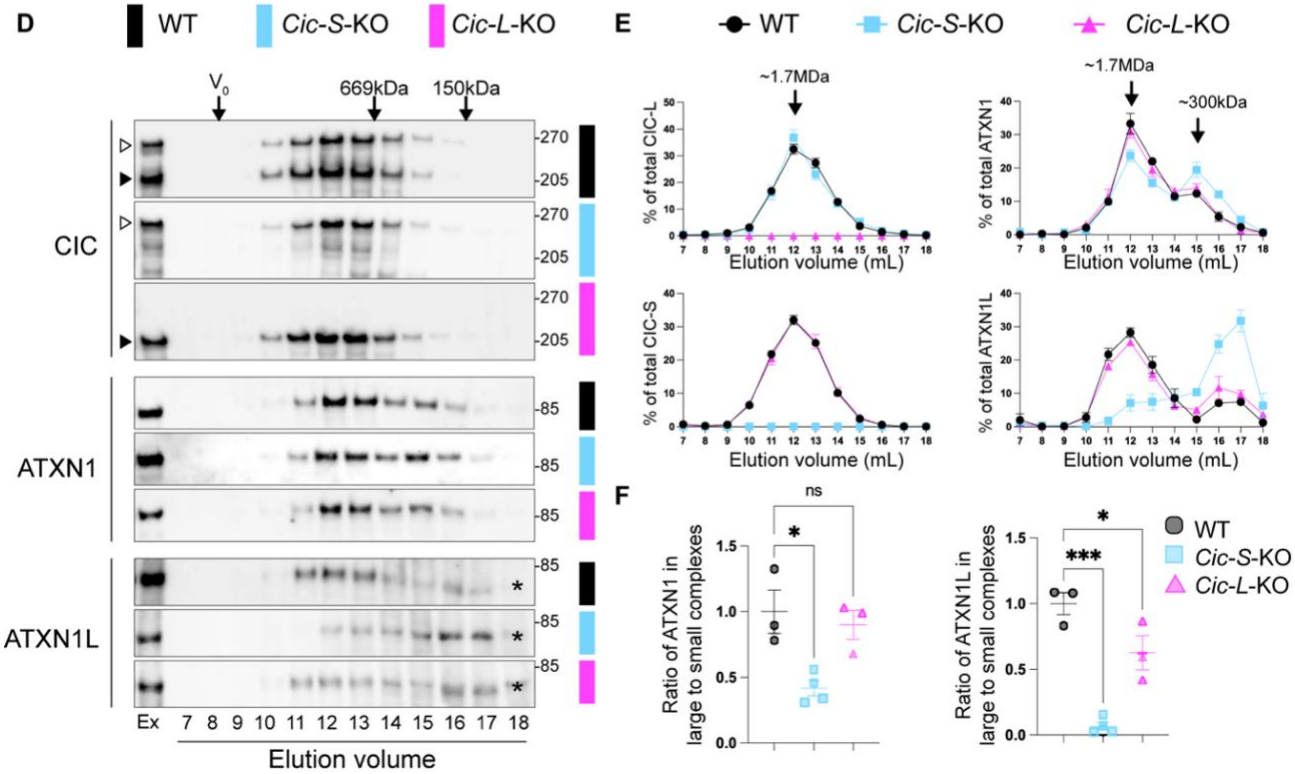
D
WT
Cic-S-KO
Cic-L-KO
V0
669kDa
150kDa
CIC
ATXN1
ATXN1L
-270
-205
-85
Ex 7 8 9 10 11 12 13 14 15 16 17 18
Elution volume
E
~1.7MDa
~300kDa
% of total CIC-L
% of total ATXN1
% of total CIC-S
% of total ATXN1L
Elution volume (mL)
F
ns
Ratio of ATXN1 in large to small complexes
Ratio of ATXN1L in large to small complexes
WT
Cic-S-KO
Cic-L-KO

873

874

875 **Figure 5. Differential complex formation of ATXN1 and ATXN1L in *Cic-S*-KO and *Cic-L*-KO in**
876 **the cortex and the cerebellum**

877 (A–C, D–F) Size exclusion chromatography (SEC) analysis of WT, *Cic-S*-KO, and *Cic-L*-KO cortex
878 (A–C) and cerebellum (D–F).

879 (A,D) Representative SEC IBs of cortex (A) and cerebellum (D) lysates probed for CIC-L, CIC-S,
880 ATXN1, and ATXN1L. Void volume (V_0), gel-filtration standards (thyroglobulin, 669 kDa; ADH,
881 150 kDa), and elution volume (ml) are indicated. Ex, extract; open arrowhead, CIC-L; closed
882 arrowhead, CIC-S; *: a nonspecific band which is observed in *Atxn1l*-KO.

883 (B,E) SEC elution profiles of indicated proteins in cortex (B) and cerebellum (E). The percentage of
884 each protein in each fraction was determined by densitometry and normalized to total signal
885 across fractions for each genotype (n = 3–4 independent extracts).

886 (C,F) Ratio of ATXN1 and ATXN1L in large versus small molecular weight fractions in cortex (C)
887 and cerebellum (F). Left: ATXN1 large (fractions 11–13) to small (fractions 15–17). Right:
888 ATXN1L large (fractions 11–13) to small (fractions 16–17). Ratios were normalized to WT. Data
889 are mean ± SEM. One-way ANOVA with Dunnett's multiple comparisons; (*) $p < 0.05$, (**) $p <$
890 0.01, (***) $p < 0.001$.

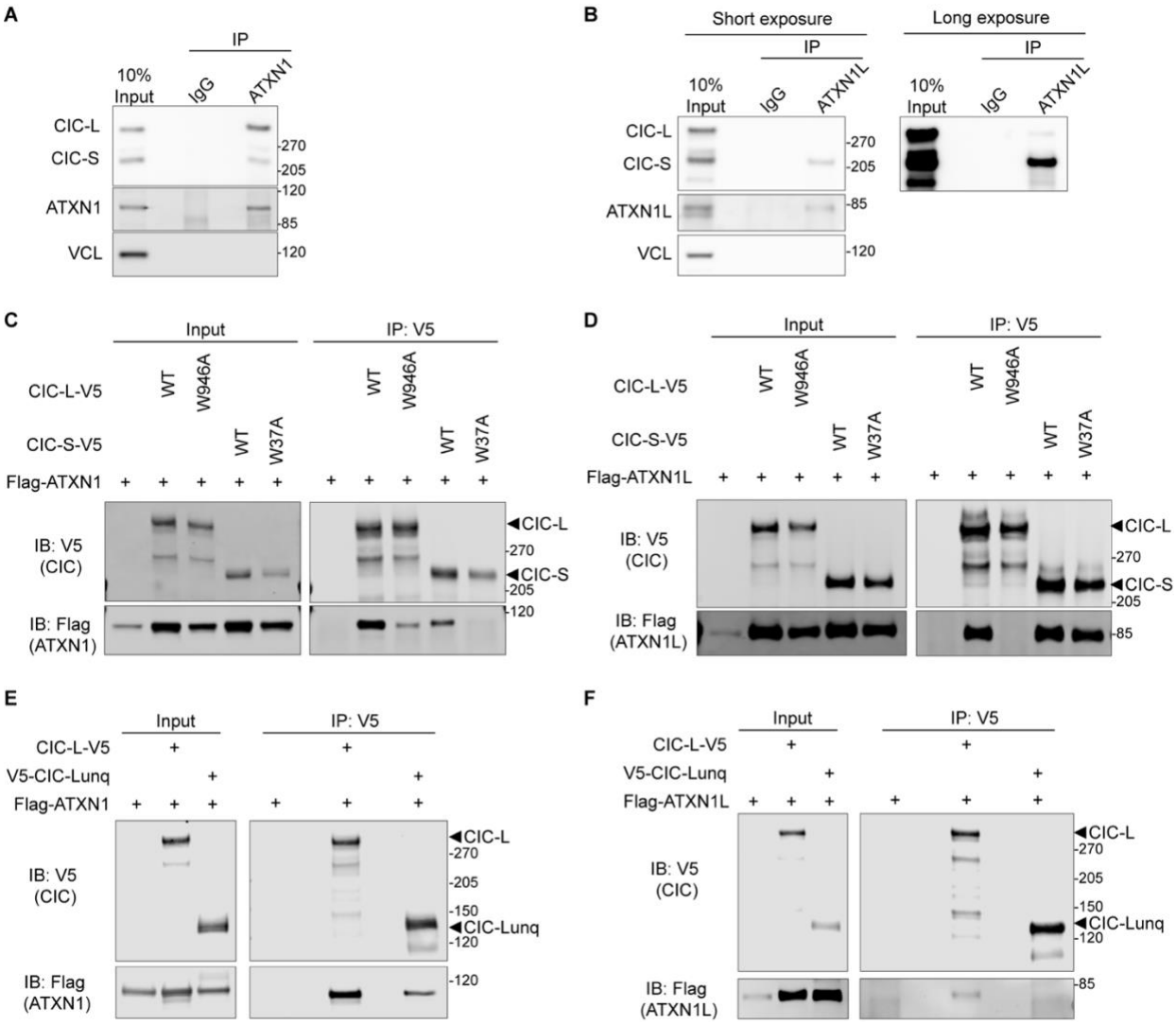
A
IP
10% Input
IgG
ATXN1
CIC-L
CIC-S
ATXN1
VCL
270
205
120
85
120
B
Short exposure
Long exposure
IP
10% Input
IgG
ATXN1L
CIC-L
CIC-S
ATXN1L
VCL
270
205
85
120
C
Input
IP: V5
CIC-L-V5
WT
W946A
CIC-S-V5
WT
W37A
Flag-ATXN1
IB: V5 (CIC)
IB: Flag (ATXN1)
CIC-L
CIC-S
270
205
120
D
Input
IP: V5
CIC-L-V5
WT
W946A
CIC-S-V5
WT
W37A
Flag-ATXN1L
IB: V5 (CIC)
IB: Flag (ATXN1L)
CIC-L
CIC-S
270
205
85
E
Input
IP: V5
CIC-L-V5
V5-CIC-Lunq
Flag-ATXN1
IB: V5 (CIC)
IB: Flag (ATXN1)
CIC-L
CIC-Lunq
270
205
150
120
120
F
Input
IP: V5
CIC-L-V5
V5-CIC-Lunq
Flag-ATXN1L
IB: V5 (CIC)
IB: Flag (ATXN1L)
CIC-L
CIC-Lunq
270
205
150
120
85

891

892

893 **Figure 6. The unique domain of each CIC isoform mediates the preferential interaction with**
894 **ATXN1 paralogs.**

895 (A, B) Representative IBs of immunoprecipitation (IP) experiments from WT cortex. IP of ATXN1
896 (A) and ATXN1L (B) and co-IPed CIC-L and CIC-S.

897 (C,D) Representative IBs of IP experiments from HEK293T co-transfected with V5-tagged CIC-L or
898 CIC-S, either WT or with an ATXN1/1L binding mutation (W946A or W37A), and Flag-tagged
899 ATXN1 (C) or ATXN1L (D). IP of V5 and co-IPed Flag.

900 (E, F) Representative IBs of IP experiments from HEK293T co-transfected with V5-tagged CIC-L or
901 CIC-L unique N-terminal (CIC-Lunq), and Flag-tagged ATXN1(C) or ATXN1L (D). IP of V5
902 and co-IPed Flag.